

Evolutionary algorithm with domain-specific operators for UAV path planning

Daison Darlan^a, Oladayo S. Ajani^b*, Rammohan Mallipeddi^a**,

^a Department of Artificial Intelligence, Kyungpook National University, South Korea

^b School of Computer Science and Engineering, Kyungpook National University, South Korea

ARTICLE INFO

Dataset link: <https://github.com/Anomaly33/Huristic-Driven-Evolutionary-UAV-Path-Planning>

Keywords:

UAV path planning

Multi-objective optimization

Autonomous navigation

ABSTRACT

Multi-objective UAV path planning is critical in practical applications such as surveillance, search-and-rescue missions, and environmental monitoring. However, the inherent complexity stemming from conflicting objectives, dynamic operational environments, and stringent mission constraints severely limits the efficacy of conventional evolutionary algorithms. Standard evolutionary operators typically fail to adequately respect domain-specific constraints, leading to infeasible or inefficient flight trajectories. Motivated by these limitations, this paper proposes specialized evolutionary operators tailored explicitly for multi-objective UAV path planning. We introduce a novel crossover operator that strategically employs the A* algorithm to generate feasible offspring paths between selected waypoints from parent solutions. Additionally, we present an adaptive polynomial mutation mechanism that dynamically controls exploration and exploitation by adjusting the mutation factor progressively across generations. Complementing this, we propose a secondary mutation operator utilizing A* to refine path segments effectively. Comprehensive ablation studies demonstrate the synergistic advantage of these innovations. Extensive evaluations on a realistic benchmark environment illustrate that our approach achieves significant enhancements, validated through substantial improvements in the hypervolume metric. Our findings confirm that embedding domain-specific intelligence into evolutionary operators markedly advances the state-of-the-art in multi-objective UAV path planning.

1. Introduction

Unmanned Aerial Vehicles (UAVs) have become integral to a diverse array of demanding applications, such as environmental surveillance [1], precision agriculture, disaster management [2], infrastructure inspection [3], and military reconnaissance [4]. Effective UAV operations critically depend on robust path-planning techniques capable of generating optimal or near-optimal trajectories while simultaneously addressing multiple conflicting objectives and stringent operational constraints. Typical path-planning objectives include minimizing travel distance, energy consumption, and flight time; maximizing area coverage; maintaining safe distances from obstacles; and ensuring robust communication links [5–7]. The inherently conflicting nature of these objectives; for instance, shorter paths potentially leading through hazardous areas versus safer but longer alternative routes renders UAV path planning a complex multi-objective optimization problem, necessitating sophisticated solution methodologies to effectively approximate diverse Pareto-optimal solutions [8,9].

Multi-objective evolutionary algorithms (MOEAs) have emerged as a prominent class of optimization methodologies for addressing such complex multi-objective scenarios. By employing biologically inspired population-based mechanisms, MOEAs iteratively evolve multiple candidate solutions, facilitating exploration of diverse trade-off solutions within a single optimization run [10,11]. Despite the widespread success and applicability of algorithms such as Non-dominated Sorting Genetic Algorithm II (NSGA-II) and Reference Vector-guided Evolutionary Algorithm (RVEA), the conventional crossover and mutation operators utilized such as Simulated Binary Crossover (SBX) and polynomial mutation remain predominantly generic, having been designed initially for broad classes of optimization problems [12,13]. Such generic operators fail to exploit inherent domain-specific structure, resulting in suboptimal performance, frequent infeasible offspring, and computational inefficiencies when applied to structured, constraint-rich problems such as UAV path planning [7,14].

Specifically, UAV path-planning problems present unique spatial and structural characteristics including explicit waypoint sequencing,

* Correspondence to: School of Computer Science and Engineering, Kyungpook National University, Daehak-ro, Buk-gu, Daegu, 41566, South Korea.

** Correspondence to: Department of Artificial Intelligence, Kyungpook National University, Daehak-ro, Buk-gu, Daegu, 41566, South Korea.

E-mail addresses: daisondarlan33@gmail.com (D. Darlan), oladayosolomon@gmail.com (O.S. Ajani), mallipeddi.ram@gmail.com (R. Mallipeddi).

complex spatial constraints, obstacle geometries, and no-fly zones, aspects typically not considered by standard evolutionary operators [15]. Consequently, traditional evolutionary operators often generate infeasible trajectories requiring extensive computational effort in post-processing repairs [9,16]. Additionally, conventional fixed-parameter mutation strategies fail to dynamically adjust mutation intensity throughout the evolutionary run, causing inadequate exploration in early stages or overly aggressive perturbations in later stages, undermining effective Pareto-front approximation [17]. Thus, the existing literature reveals an urgent requirement for specialized evolutionary operators tailored explicitly to UAV path planning, incorporating domain-specific heuristics and adaptive strategies to ensure feasibility, accelerate convergence, and optimize solution quality.

Recent literature has indeed begun exploring domain-specific evolutionary operators; however, efforts remain fragmented and typically limited to simplified environments or specific mission scenarios. Problem-specific crossovers integrating obstacle-aware heuristics have demonstrated promising results in robotics and UAV contexts [6,15], while adaptive mutation strategies adjusting mutation intensity dynamically have exhibited improved performance in standard multi-objective benchmarks [7,17]. Nevertheless, the integration of domain-specific heuristics and adaptive operators within comprehensive multi-objective frameworks tailored explicitly to realistic UAV routing scenarios remains largely under-investigated. This gap motivates the present work.

In response, this paper proposes a multi-objective evolutionary algorithm explicitly tailored for UAV path-planning problems by embedding the classical heuristic-driven A* pathfinding algorithm [18] directly into both crossover and mutation operators. Our proposed A*-guided crossover operator strategically selects intermediate waypoints from two parent solutions, utilizing A* search to generate collision-free, locally optimized connecting subpaths. By directly embedding obstacle-awareness and environmental constraints into offspring generation, this approach inherently ensures offspring feasibility, significantly reducing the need for computationally intensive feasibility repairs. Concurrently, the A*-guided mutation operator identifies and replaces inefficient or infeasible subsegments within candidate solutions through local A*-based path replanning. This targeted approach systematically improves solution feasibility and quality, continually guiding the population toward structurally promising search regions. To complement these domain-specific operators, we further introduce a dynamically controlled polynomial mutation mechanism, adaptively varying the distribution index across generations. Initially employing broader, exploratory mutations to maximize search-space coverage, this adaptive scheme transitions progressively to narrower perturbations, refining solutions as the evolutionary process advances toward convergence. This approach systematically addresses the classical exploration-exploitation trade-off, maintaining population diversity while effectively intensifying convergence toward the Pareto-optimal front.

Rigorous empirical validation of our proposed methods is conducted using recently developed realistic UAV path-planning benchmarks, specifically incorporating complex obstacle layouts, varied terrain, and stringent operational constraints, as proposed by [19]. This benchmark comprises 14 systematically designed scenarios categorized into three distinct environmental settings: urban, suburban, and mountainous. Each scenario category features unique complexities and constraints, closely mirroring realistic UAV operational conditions. Comparative performance studies against established algorithms including NSGA-II/SDR [20], HypE [21], I_{SDE+} [22], MOEA-2DE [6] and MOEA/D-AWA [23] demonstrate the significant superiority of our domain-specific and adaptive operators, evidenced by marked improvements in hypervolume indicator values, convergence rates, and Pareto-front diversity.

In summary, the primary technical contributions of this paper are as follows:

- **A*-guided crossover operator:** Development of a specialized recombination method embedding the A* heuristic directly within evolutionary crossover, explicitly incorporating obstacle and feasibility constraints, thereby generating inherently feasible and structurally superior offspring solutions and substantially mitigating the computational burden associated with solution repairs.
- **A*-guided mutation operator:** Introduction of a targeted mutation approach leveraging A* search for local replanning of trajectory segments, systematically replacing infeasible or inefficient route sections with feasible, optimized alternatives, thus enhancing both solution feasibility and evolutionary convergence.
- **Adaptive polynomial mutation control:** Formulation of a generation-dependent adaptive strategy for polynomial mutation, dynamically balancing exploration and exploitation through controlled variation of the mutation distribution index. This mechanism significantly enhances solution diversity during early generations and promotes precise exploitation and convergence refinement at later evolutionary stages.
- **Comprehensive empirical validation:** Rigorous performance evaluation on realistic UAV path-planning benchmarks, conclusively demonstrating superior solution quality and accelerated convergence compared to state-of-the-art multi-objective evolutionary algorithms.

The remainder of this paper is organized as follows. Section 2 reviews the related work on multi-objective UAV path planning and domain-specific approaches in literature. Section 3 summarizes the theoretical fundamentals of multi-objective optimization, UAV path representation, and evaluation criteria that ground the proposed approach. Section 4 details the proposed methodology, introducing the A*-guided waypoint-connecting crossover, the A*-guided mutation, and the generation-controlled adaptive polynomial mutation within the MOEA/D-AWA framework. Section 5 describes the experimental study, including the 14-scenario benchmark suite, baseline algorithms, performance metrics, and all implementation specifics. Section 6 reports and discusses the empirical results, presenting convergence curves, ablation analyses, and trajectory visualizations. Finally, Section 7 concludes the paper and outlines avenues for future research.

2. Related work

Multi-objective evolutionary algorithms (MOEAs) have been widely adopted in UAV path-planning scenarios, given their intrinsic capability to simultaneously optimize multiple conflicting objectives, such as minimizing flight distance, energy consumption, and collision risks [6, 24]. Among these, Pareto-based algorithms, notably NSGA-II [10], and decomposition-based methods such as MOEA/D [11], have consistently demonstrated strong performance. NSGA-II, for instance, has been effectively adapted to urban and obstacle-rich mountainous environments by explicitly handling collision avoidance and path-length constraints [24,25]. Similarly, adaptive variants of MOEA/D, incorporating dynamic weight adjustment schemes, have been shown to balance competing UAV mission objectives such as total travel distance and threat exposure effectively [26]. In recent years, the field has seen a surge of advanced frameworks that further improve search efficiency and adaptability. A global-local collaborative decomposition-based algorithm for 3-D UAV path planning [27] and the EMOA* framework for search-based multi-objective path planning [28] exemplify the trend toward hybrid designs combining heuristic exploration with deterministic guidance. Other studies have enhanced constraint handling and diversity preservation, such as the two-fold constraint-handling strategy for multi-UAV cooperative missions [29] and two-stage co-evolutionary optimization for real-time trajectory generation [30]. Reinforcement-learning-based planners have also emerged, integrating environmental awareness and post-disaster adaptability into decision-making [31,32].

Despite these advancements, the predominant reliance on generic evolutionary operators like Simulated Binary Crossover (SBX) and polynomial mutation limits their applicability in complex UAV routing problems, often resulting in infeasible trajectories that require computationally intensive feasibility repairs [7,16]. Consequently, there has been significant interest in designing domain-specific evolutionary operators that inherently integrate UAV-specific structural knowledge, including waypoint sequences, obstacle maps, terrain profiles, and dynamic constraints, to directly ensure solution feasibility and enhance convergence properties [33,34]. Specifically, specialized crossover operators that embed domain-specific heuristics have garnered attention. For example, waypoint-based recombination techniques [34] and hybrid evolutionary-Dijkstra approaches [35] explicitly ensure obstacle avoidance and feasibility during offspring generation. Such strategies substantially reduce the computational overhead associated with post-processing infeasible solutions. Similarly, targeted mutation strategies such as knowledge-based waypoint manipulation [36], localized heuristic-based segment replacement [34], and directional perturbations toward known feasible or promising solution regions [37] have been developed, systematically improving path continuity and constraint compliance compared to traditional stochastic perturbation operators.

In parallel, recent evolutionary frameworks have explored adaptive mutation mechanisms to dynamically modulate mutation intensities based on evolving population characteristics or real-time performance metrics [38,39]. These adaptive schemes aim to balance exploration and exploitation effectively; however, their practical deployment often involves significant complexity, including runtime monitoring, additional parameter tuning, and feedback-based adjustments, thus reducing their operational feasibility in realistic UAV scenarios [40, 41].

In contrast to these existing approaches, the current study uniquely integrates the heuristic-driven A* algorithm directly into the evolutionary operators themselves. Specifically, the proposed *A*-guided crossover* operator recombines parent trajectories through deterministic obstacle-aware bridging via the A* algorithm, inherently guaranteeing solution feasibility and significantly reducing the overhead associated with subsequent feasibility checks or repairs. Complementing this, our *A*-guided mutation* explicitly targets and replaces inefficient or infeasible sub-path segments by performing local A*-based replanning, systematically improving path quality and feasibility. Furthermore, to address the drawbacks of traditional fixed-parameter mutation and more complex adaptive mechanisms, we propose a generation-dependent adaptive polynomial mutation strategy, adjusting the mutation intensity deterministically across generations. This structured approach ensures broad exploration early in the evolutionary run, progressively narrowing perturbation intensity as convergence is achieved, effectively balancing exploration and exploitation without incurring additional runtime complexity. Together, these methodological innovations distinctly position our proposed framework as a comprehensive, practically viable, and robust solution for multi-objective UAV path planning, effectively addressing critical limitations identified in previous evolutionary approaches.

3. Background

3.1. Multi-objective optimization (MOO)

Multi-objective optimization (MOO) addresses problems involving multiple conflicting objectives. In contrast to single-objective optimization (SOO), where a unique optimal solution is identified by comparing objective function values, MOO often leads to a set of solutions rather than a single optimum. This is due to the complexity of optimizing several objectives simultaneously, where improving one objective may cause deterioration in others.

A general mathematical formulation for MOO can be represented as follows:

$$\begin{aligned} \min / \max \quad & f_m(\mathbf{x}), \quad m = 1, 2, \dots, M \\ & x_i^{\text{lower}} \leq x_i \leq x_i^{\text{upper}}, \quad i = 1, 2, \dots, n \end{aligned} \quad (1)$$

Here, M denotes the number of objective functions given by $f_m(\mathbf{x})$. The decision variables, \mathbf{x} are bounded within upper and lower limits for each variable, x_i^{lower} and x_i^{upper} where n is the total number of decision variables.

In multi-objective problems (MOPs), it is often impossible to find the “best” or optimum solution that optimizes all the objectives simultaneously. This is because, due to the conflicting nature of objectives in the MOP, a solution that has the highest value for a certain objective will inevitably not have the best value for another objective. Instead, solutions are often evaluated based on the concept of dominance. A solution \mathbf{x}_1 is said to dominate another solution \mathbf{x}_2 if it is at least as good in all objectives and strictly better in at least one objective. Mathematically,

$$\forall m \in 1, 2, \dots, M, \quad f_m(\mathbf{x}_1) \leq f_m(\mathbf{x}_2), \quad (2)$$

and

$$\exists m \in 1, 2, \dots, M, \quad f_m(\mathbf{x}_1) < f_m(\mathbf{x}_2) \quad (3)$$

The set of non-dominated solutions forms the Pareto front, which represents the trade-offs between competing objectives. Users can select their preferred solution based on their needs and the relative importance of the objectives, choosing from the Pareto front rather than settling for a single optimum as in SOO.

Multi-objective evolutionary algorithms (MOEAs) have become prominent tools for addressing MOO problems, especially in complex UAV path-planning tasks. These algorithms approximate diverse Pareto-optimal solutions through population-based searches. Prominent categories of MOEAs include Pareto-based methods (e.g., Non-dominated Sorting Genetic Algorithm II (NSGA-II) [10]), decomposition-based methods (e.g., Multi-Objective Evolutionary Algorithm based on Decomposition (MOEA/D) [11]), indicator-based methods (e.g., Hypervolume Estimation Algorithm (HypE) [21]), and swarm intelligence-based methods (e.g., Multi-objective Particle Swarm Optimization (MOPSO) [42]). MOEA/D decomposes multi-objective optimization into concurrent scalar subproblems, demonstrating strength in high-dimensional optimization, though it requires careful parameter tuning for irregular or highly constrained problems. MOEA/D-AWA [23] improves upon MOEA/D by adaptively adjusting subproblem weights throughout the evolutionary process. Recent studies highlight MOEA/D-AWA’s superior performance in UAV path planning involving dense obstacles, complex urban landscapes, and altitude variations [19,43].

Although the proposed evolutionary operators discussed later in this paper can theoretically be integrated into various multi-objective evolutionary algorithms, this study employs the MOEA/D-AWA framework to evaluate our domain-specific operators. The selection of MOEA/D-AWA is justified by its adaptive weighting mechanism, which dynamically adjusts subproblem weights during optimization, providing a balanced exploration and exploitation strategy. Additionally, MOEA/D-AWA’s proven effectiveness and robust performance across diverse UAV planning benchmarks, especially in complex and constraint-rich environments, further support its adoption. This ensures a comprehensive and rigorous assessment of the proposed heuristic-driven crossover and mutation operators.

3.2. Path representation and smoothing

In this research, UAV path planning utilizes a structured grid-based spatial representation. Specifically, the environment is discretized into

uniform grids along three axes ($\Delta x, \Delta y, \Delta z$), creating a structured framework for accurately representing UAV positions and potential trajectories within a 3D operational space. Each discrete grid point is denoted by coordinates (x_i, y_i, z_i) , enabling precise definition of waypoints along the UAV trajectory. Consequently, a UAV path can be explicitly represented as an ordered sequence of N discrete waypoints:

$$P = \{(x_1, y_1, z_1), (x_2, y_2, z_2), \dots, (x_N, y_N, z_N)\}. \quad (4)$$

Direct traversal between these discrete waypoints, however, typically results in abrupt trajectory changes, posing navigation inefficiencies and impracticalities. To mitigate these issues and enhance operational feasibility, the discrete waypoint path undergoes smoothing via interpolation techniques. In particular, B-spline interpolation is chosen due to its proven effectiveness in generating smooth and dynamically feasible trajectories from discrete control points, balancing computational efficiency with trajectory flexibility [44–46].

Given a sequence of discrete control points $\mathbf{P}_i = (x_i, y_i, z_i)$, a B-spline curve of degree d is generated to produce a smooth UAV trajectory. Mathematically, the B-spline interpolation curve $C(u)$ is defined as:

$$C(u) = \sum_{i=0}^m \mathbf{P}_i N_{i,d}(u), \quad u \in [0, 1], \quad (5)$$

where \mathbf{P}_i denotes control points, $N_{i,d}(u)$ are the B-spline basis functions of degree d , and $(m+1)$ is the total number of control points.

The basis functions $N_{i,d}(u)$ are computed recursively based on knot values t_i as follows:

$$N_{i,0}(u) = \begin{cases} 1, & t_i \leq u < t_{i+1}, \\ 0, & \text{otherwise,} \end{cases} \quad (6)$$

and for higher-order functions:

$$N_{i,d}(u) = \frac{u - t_i}{t_{i+d} - t_i} N_{i,d-1}(u) + \frac{t_{i+d+1} - u}{t_{i+d+1} - t_{i+1}} N_{i+1,d-1}(u). \quad (7)$$

A uniform knot vector placement is consistently employed, ensuring simplicity and computational efficiency without compromising adaptability to complex terrain scenarios.

3.3. Path evaluation and constraints

Evaluating UAV trajectories is fundamental to ensuring operational efficacy and efficiency. Typically, trajectory quality is assessed by criteria such as path length, altitude profiles, and energy consumption. Explicit modeling of UAV energy consumption can be computationally intensive; thus, energy consumption is efficiently approximated using path length and altitude—parameters that significantly influence UAV energy requirements:

$$E_{\text{approx}} = k_L L + k_H H_{\text{avg}}, \quad (8)$$

where k_L and k_H are coefficients reflecting UAV-specific and environmental characteristics, L denotes total path length, and H_{avg} denotes average flight altitude across all waypoints. Since the UAV's energy consumption can be effectively approximated by its path length and average flight altitude, these two factors are adopted as the optimization objectives. Accordingly, the path-planning task is formulated as a bi-objective problem that seeks to minimize both total path length and average path height. These objectives are inherently conflicting: minimizing path length often favors lower-altitude trajectories that cut closer to terrain or obstacles, while maintaining higher altitudes improves safety and reduces the risk of collisions but increases overall energy expenditure.

The total path length L is computed explicitly as the cumulative Euclidean distance between consecutive waypoints:

$$L = \sum_{i=1}^{N-1} \sqrt{(x_{i+1} - x_i)^2 + (y_{i+1} - y_i)^2 + (z_{i+1} - z_i)^2}. \quad (9)$$

Minimizing path length directly reduces flight duration and associated energy costs. The average flight altitude is

$$H_{\text{avg}} = \frac{1}{N} \sum_{i=1}^N z_i, \quad (10)$$

and impacts both energy usage and collision risk.

Beyond efficiency, candidate trajectories must satisfy feasibility constraints. Maximum altitude limits prevent conflicts with airspace ceilings,

$$z_i \leq h_{\text{max}}^{\text{UAV}}, \quad \forall i \in \{1, \dots, N\}, \quad (11)$$

while terrain clearance and obstacle avoidance ensure safety,

$$z_i \geq h_i^{\text{terrain}} + h_{\text{safe}}, \quad \mathcal{O}(x_i, y_i) = 0 \quad \forall i, \quad (12)$$

where h_i^{terrain} is the local terrain height and \mathcal{O} is an occupancy mask for obstacles and no-fly zones. Kinematic limits further preserve flight stability, with horizontal and vertical turning angles constrained as

$$\begin{aligned} \theta_h &= \arccos\left(\frac{\mathbf{v}_i \cdot \mathbf{v}_{i-1}}{\|\mathbf{v}_i\| \|\mathbf{v}_{i-1}\|}\right) \leq \theta_h^{\max}, \\ \theta_v &= \arccos\left(\frac{\mathbf{u}_i \cdot \mathbf{u}_{i-1}}{\|\mathbf{u}_i\| \|\mathbf{u}_{i-1}\|}\right) \leq \theta_v^{\max}. \end{aligned} \quad (13)$$

where $\mathbf{v}_i = (x_i - x_{i-1}, y_i - y_{i-1})$ denotes the horizontal velocity vector projected onto the xy -plane between consecutive waypoints, and $\mathbf{u}_i = (\|\mathbf{v}_i\|, z_i - z_{i-1})$ denotes the corresponding vertical motion vector capturing climb and descent between waypoints.

Feasibility is enforced both during evaluation and through localized repair of any trajectory segments that violate geometric or environmental constraints. Each waypoint is first projected onto the valid planar domain to ensure it lies within map boundaries, and its altitude is adjusted to maintain terrain clearance. Specifically, the waypoint altitude is redefined as

$$z_i = \max_{(x', y') \in \mathcal{N}(x_i, y_i)} h^{\text{terrain}}(x', y') + h_{\text{safe}}, \quad (14)$$

where $\mathcal{N}(x_i, y_i)$ denotes a small spatial neighborhood around the waypoint (x_i, y_i) . This formulation guarantees that every waypoint satisfies the minimum safety margin h_{safe} above the highest local terrain elevation. Horizontal turning-angle violations are corrected by perturbing the in-plane coordinates of the offending waypoint within a bounded neighborhood until the angular constraint $\theta_h \leq \theta_h^{\max}$ is met, while vertical turning-angle violations are repaired by redistributing the altitude between adjacent waypoints to reduce the local slope such that $\theta_v \leq \theta_v^{\max}$. These repair operations are conservative, modifying only the minimal number of waypoints required to restore feasibility and preserve the overall trajectory geometry. Additionally, as detailed in Section 4, obstacle-aware local replanning based on A* search is invoked during crossover and mutation, ensuring that newly generated path segments remain collision-free by construction. The combined use of constraint repair and local replanning allows the proposed framework to consistently generate feasible, smooth, and energy-efficient UAV trajectories across diverse terrains.

3.4. A* search algorithm

For local path refinement, the A* algorithm [18] is applied on the discretized 3D occupancy grid $G = (V, E)$, where each node $v \in V$ denotes a free voxel and each edge $e = (u, v) \in E$ carries a traversal cost $c(u, v)$ (e.g., Euclidean step length or energy proxy).

A* evaluates nodes using

$$f(v) = g(v) + h(v), \quad (15)$$

where $g(v)$ is the accumulated cost from the start node and $h(v)$ is the heuristic estimate to the goal. For UAV planning, $h(v)$ is defined as the Euclidean distance:

$$h(v) = \sqrt{(x_{\text{goal}} - x_v)^2 + (y_{\text{goal}} - y_v)^2 + (z_{\text{goal}} - z_v)^2}. \quad (16)$$

This admissible heuristic ensures completeness and optimality. The search expands nodes in order of increasing $f(v)$ until the goal is reached, after which the optimal path is reconstructed as

$$P^* = \arg \min_{P \in \mathcal{P}} \sum_{i=1}^{|P|-1} c(v_i, v_{i+1}). \quad (17)$$

Within the developed framework, A* serves as a local repair operator: (i) to connect waypoints during crossover and (ii) to refine perturbed segments during mutation. This guarantees feasibility and injects locally optimal structure into evolving trajectories.

3.5. Polynomial mutation and the η -parameter

Polynomial mutation is a standard evolutionary operator commonly employed in real-valued evolutionary algorithms and multi-objective optimization methods such as NSGA-II [10]. Its primary purpose is to maintain diversity within the population by introducing small, controlled perturbations to the decision variables. Unlike random or uniform perturbation schemes, polynomial mutation applies a distribution characterized explicitly by a polynomial probability density function, providing fine-grained control over the mutation magnitude.

Given a decision variable x_i with permissible bounds $[x_i^{\min}, x_i^{\max}]$, polynomial mutation generates a mutated variable x'_i according to the rule:

$$x'_i = x_i + \delta_i(x_i^{\max} - x_i^{\min}), \quad (18)$$

where the perturbation factor δ_i is derived from the following polynomial distribution [10]:

$$\delta_i = \begin{cases} (2u)^{\frac{1}{\eta+1}} - 1, & \text{if } u < 0.5 \\ 1 - [2(1-u)]^{\frac{1}{\eta+1}}, & \text{otherwise} \end{cases} \quad (19)$$

with u drawn uniformly at random from the interval $[0, 1]$. After calculating δ_i , the mutated value x'_i is clipped, to remain within the specified bounds:

$$x'_i = \min(\max(x'_i, x_i^{\min}), x_i^{\max}). \quad (20)$$

Central to the polynomial mutation operator is the distribution index parameter η , which directly governs the shape and spread of the mutation distribution. Specifically, the parameter η modulates the mutation step size as follows:

- A smaller η value produces a broader (heavy-tailed) distribution, resulting in larger mutation steps and thus encouraging exploration of the search space.
- Conversely, a larger η concentrates mutations tightly around the current value, favoring exploitation and local refinement [47].

Mathematically, the probability distribution defined by Eq. (19) ensures symmetry around the current decision variable x_i , with the spread determined by η . For instance, setting $\eta = 1$ results in a distribution with higher probability for larger perturbations (more exploratory), while setting $\eta \approx 20$, as often recommended in practice, yields predominantly minor perturbations (more exploitative) [10,47].

Several studies have explored alternative strategies for adapting the mutation distribution parameter dynamically. [48] developed a self-adaptive polynomial mutation within NSGA-II, where the distribution index evolves alongside the solution population, automatically adjusting to different optimization scenarios. Similarly, [17,47] investigated dynamically varying the distribution index over the evolutionary run, observing improved convergence and diversity outcomes in comparison to fixed-parameter approaches. Other methods, such as the q-Gaussian mutation and the heavy-tailed mutation distributions have also demonstrated the effectiveness of adaptive mutation control in various optimization problems [49,50].

Within the context of UAV multi-objective path planning, polynomial mutation is particularly relevant due to the delicate balance it offers between exploring novel route alternatives and exploiting local trajectory refinements. Properly managing this trade-off through the careful tuning of the η parameter is crucial for achieving high-quality solutions. As will be detailed later in this paper, adopting a dynamic, generation-based schedule for η enables a systematic transition from broad exploration in early evolutionary stages to precise exploitation as the search converges toward Pareto-optimal trajectories.

4. Proposed methodology

The methodological contribution of this work lies in embedding path-planning heuristics directly into the variation operators of the MOEA framework. First, the *waypoint-connecting crossover* selects one interior control point from each parent path, then uses an A* search to build a collision-free bridge between them. This bridge replaces the corresponding segment and the resulting trajectory is uniformly re-sampled to produce the offspring. Second, an *A*-guided mutation* replaces inefficient or infeasible sub-segments by executing a bounded A* replanning procedure between two randomly selected interior waypoints, thereby guaranteeing post-mutation feasibility while imparting deterministic local improvement. Finally, a *generation-dependent polynomial mutation* dynamically anneals the distribution index $\eta(g)$, beginning with a heavy-tailed kernel that promotes global exploration and gradually narrowing toward a fine-tuning regime as the search progresses. These operators are integrated into MOEA without altering its neighborhood, or environmental-selection mechanisms, ensuring that any observed performance gains can be attributed solely to the proposed domain-specific variation operators. To actively enforce obstacle avoidance during search, both the waypoint-connecting crossover and the local mutation invoke an A* planner on the grid map to replan the edited sub-segments; thus, any new segment inserted by the operators is collision-free by construction (see Algorithms 1–2). The following subsections present the mathematical formulation and algorithmic realization of each component, culminating in Algorithm 3, which summarizes their organization within the evolutionary cycle.

4.1. Waypoint-connecting crossover

The waypoint-connecting crossover we introduce weaves deterministic path-planning intelligence into the otherwise stochastic recombination process of a multi-objective EA. As depicted in Fig. 1, each parent trajectory is a length- N chromosome, $\mathbf{P}_A = \{\mathbf{p}_A^1, \dots, \mathbf{p}_A^N\}$ and $\mathbf{P}_B = \{\mathbf{p}_B^1, \dots, \mathbf{p}_B^N\}$, whose control points are subsequently joined by a cubic B-spline to yield smooth, dynamically feasible flight paths. After the two parents have been selected by binary tournament, the operator samples, with uniform probability, one interior control-point index i from $\{2, \dots, N-1\}$ in \mathbf{P}_A and another index j from the same range in \mathbf{P}_B . These indices identify the waypoints $\mathbf{w}_A = \mathbf{p}_A^i$ and $\mathbf{w}_B = \mathbf{p}_B^j$, which form the termini of a local replanning sub-problem.

Both waypoints are first projected onto the closest cells of the environment grid, yielding `startCell` and `goalCell`. An A* search is then invoked to construct a collision-free cell sequence $\{c_k\}_{k=1}^M$. During expansion the algorithm evaluates each candidate cell c with

$$F(c) = G(c) + H(c), \quad (21)$$

where the cost-to-come

$$G(c) = \sum_{\ell=1}^{k-1} \|c_{\ell+1} - c_{\ell}\|_2 \quad (22)$$

accumulates exact path length, and the heuristic

$$H(c) = \|c - \text{goalCell}\|_2 \quad (23)$$

is the admissible Euclidean estimate to the goal. If the forward query $(\mathbf{w}_A \rightarrow \mathbf{w}_B)$ is blocked, the search is automatically repeated in the

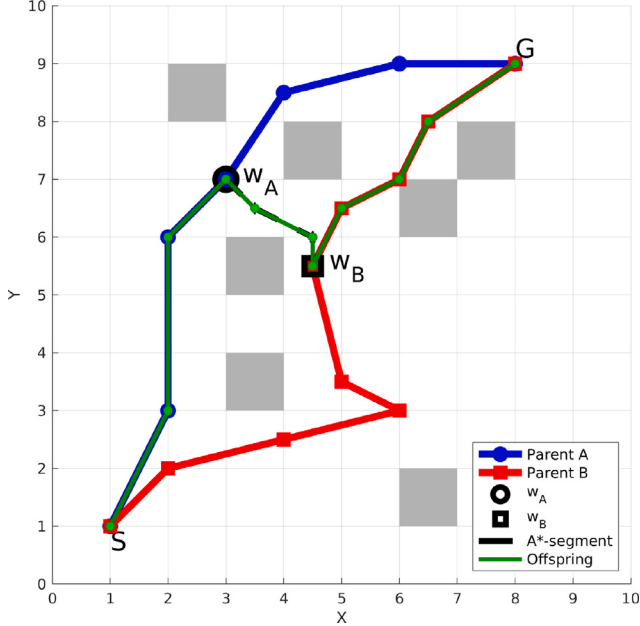


Fig. 1. 2D Visualization of the waypoint-connecting crossover: two parent trajectories (blue/red), selected waypoints W_A, W_B (black markers), A*-computed bridge (dashed line), and resulting offspring (green) after uniform resampling to N control points. (For interpretation of the references to color in this figure legend, the reader is referred to the web version of this article.)

reverse direction, providing additional robustness in heavily cluttered airspaces.

The discrete route is next lifted back to continuous space. For each grid cell c_k we recover its world coordinates $(x(c_k), y(c_k))$ and interpolate altitude linearly between the end-point heights z_A and z_B :

$$Q_k = (x(c_k), y(c_k), (1 - t_k)z_A + t_k z_B), \quad t_k = \frac{k-1}{M-1}. \quad (24)$$

The set $\{Q_k\}_{k=1}^M$ therefore realizes a continuous, obstacle-aware bridge from w_A to w_B .

Offspring synthesis proceeds by concatenating the prefix of Parent A up to w_A , the interior bridge $\{Q_2, \dots, Q_{M-1}\}$, and the suffix of Parent B beginning with w_B :

$$\mathbf{P}_{\text{child}} = \{\mathbf{p}_A^1, \dots, \mathbf{p}_A^i, Q_2, \dots, Q_{M-1}, \mathbf{p}_B^j, \dots, \mathbf{p}_B^N\}. \quad (25)$$

Because this list may contain more or fewer than N points, the composite trajectory is re-parameterized by arc length $\Gamma(s)$, $s \in [0, S]$ and uniformly resampled

$$\mathbf{P}_{\text{child}}^{\text{unif}}(k) = \Gamma\left(\frac{k-1}{N-1}S\right), \quad k = 1, \dots, N, \quad (26)$$

maintaining a genome length consistent with the remainder of the evolutionary framework.

Embedding A* inside the crossover delivers a key advantage: it allows the algorithm to splice locally shortest or lower-altitude fragments from each parent into a single, continuous route that neither parent explored in full. Because the bridge is found by an informed search over the environment graph, it can exploit gaps between obstacles or valleys in the terrain that a purely algebraic recombination would overlook. Traditional real-coded operators, such as SBX, mix coordinates component-wise according to $\tilde{\mathbf{p}} = \beta \mathbf{p}_A + (1 - \beta) \mathbf{p}_B$ with β drawn from a unimodal distribution. Although this convex blending preserves continuity in \mathbb{R}^n , it ignores the sequential structure of waypoints: intermediate points produced by SBX have no guarantee of lying in free space, nor do they respect obstacles, no-fly zones, or altitude corridors. Any infeasibility must therefore be repaired after the fact, often by expensive re-routing or rejection.

In contrast, the proposed operator performs its optimization within the crossover step as detailed in Algorithm 1. Random selection of w_A and w_B injects global diversity, while the A* planner supplies deterministic, obstacle-aware local search that guarantees a collision-free bridge. Executing the search in both directions — $w_A \rightarrow w_B$ and, if necessary, $w_B \rightarrow w_A$ — adds robustness in highly constrained airspaces. The linear altitude interpolation of Eq. (24) then removes vertical discontinuities, ensuring the stitched route remains compatible with fixed-wing or rotary-wing performance envelopes. Finally, uniform resampling enforces a fixed chromosome length, preserving compatibility with subsequent genetic operators without diluting the geometric fidelity of the newly synthesized path. By fusing stochastic exploration with deterministic, environment-informed exploitation in a single step, the waypoint-connecting crossover provides a principled, constraint-respecting alternative to classical arithmetic recombination schemes in UAV trajectory optimization.

Algorithm 1: Waypoint-Connecting Crossover with A*-Guided Bridging

Input: Parent chromosomes $\mathbf{P}_A, \mathbf{P}_B$, terrain grid G , control points number N
Result: Offspring chromosome \mathbf{C}

- 1 $\mathbf{C} \leftarrow \emptyset;$
- 2 Randomly select interior indices $i \in \{2, \dots, N-1\}$ from \mathbf{P}_A and $j \in \{2, \dots, N-1\}$ from \mathbf{P}_B ;
- 3 Extract waypoints $W_A \leftarrow \mathbf{P}_A(i)$, $W_B \leftarrow \mathbf{P}_B(j)$;
- 4 Map waypoints W_A, W_B to nearest grid cells (startCell, goalCell);
- 5 **if** A* search from startCell to goalCell succeeds **then**
- 6 | Set discrete path cells \mathcal{P} as resulting A* path;
- 7 **end**
- 8 **else if** A* search from goalCell to startCell succeeds **then**
- 9 | Set discrete path cells \mathcal{P} as reversed resulting A* path;
- 10 **end**
- 11 **else**
- 12 | **return** \emptyset (*No feasible offspring*)
- 13 **end**
- 14 Convert discrete grid path \mathcal{P} to continuous coordinates using linear altitude interpolation between W_A and W_B ;
- 15 Create offspring chromosome \mathbf{C} by concatenating segments: $\mathbf{P}_A(1 : i)$, interpolated bridge, and $\mathbf{P}_B(j : N)$;
- 16 Uniformly resample \mathbf{C} to exactly N control points;
- 17 **return** \mathbf{C} ;

4.2. A*-guided mutation operator

Mutation operators play a crucial role in evolutionary algorithms by maintaining diversity within the population and preventing premature convergence. Conventional mutation strategies often introduce random perturbations that may lead to infeasible or suboptimal trajectories, particularly in constrained UAV path-planning scenarios. To address these limitations, we propose an A*-guided mutation operator, which systematically ensures solution feasibility and enhances local optimality through targeted modifications.

Given a candidate chromosome represented by a set of control points $\mathbf{P} = \{P_1, P_2, \dots, P_N\}$, the mutation process follows the steps detailed in Algorithm 2. Firstly, two distinct interior control points P_i and P_j are randomly selected, with indices satisfying $1 < i < j < N$. These selected points delineate the segment of the trajectory targeted for mutation. The spatial coordinates of these points, (x_i, y_i) and (x_j, y_j) , are discretized onto the terrain model grid G , producing the start and goal cells for the mutation:

$$\text{startCell} = \text{gridMap}(P_i), \quad \text{goalCell} = \text{gridMap}(P_j). \quad (27)$$

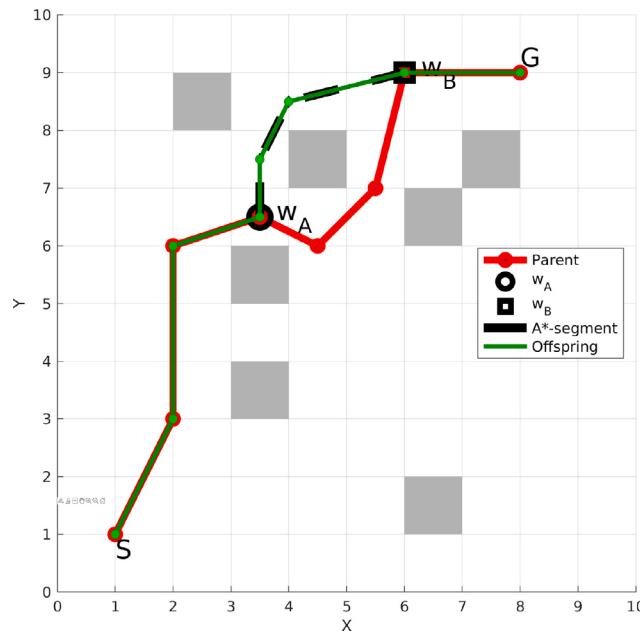


Fig. 2. Visualization of the A*-guided mutation operator: selected mutation segment from waypoint W_A to W_B , the optimal sub-path generated by A* (black dashed line), and resulting mutated offspring (green). (For interpretation of the references to color in this figure legend, the reader is referred to the web version of this article.)

To optimize computational resources and enhance search efficiency, a localized bounding box is defined around these two selected grid cells. The bounding region restricts the search area, significantly reducing computational overhead without compromising search quality. Given a predefined radius R , the bounding box limits are defined as:

$$\begin{aligned} \text{row}_{\min, \max} &= [\min(y_i, y_j) - R, \max(y_i, y_j) + R], \\ \text{col}_{\min, \max} &= [\min(x_i, x_j) - R, \max(x_i, x_j) + R]. \end{aligned} \quad (28)$$

Within this constrained search region, the A* algorithm computes an optimal, obstacle-free discrete path between the start and goal cells. The discrete A* search operates by iteratively selecting grid cells based on a cost function $F(c)$:

$$F(c) = G(c) + H(c), \quad (29)$$

where $G(c)$ denotes the accumulated path cost from the start cell to the current cell c , and $H(c)$ is an admissible heuristic defined as the Euclidean distance from cell c to the goal cell:

$$H(c) = \sqrt{(x_c - x_{\text{goal}})^2 + (y_c - y_{\text{goal}})^2}. \quad (30)$$

Upon identifying the optimal discrete path $\mathcal{P} = \{c_1, c_2, \dots, c_M\}$, it is mapped back into continuous space by performing linear interpolation of altitudes between the selected control points P_i and P_j :

$$Z(c_k) = Z(P_i) + \frac{k-1}{M-1} (Z(P_j) - Z(P_i)). \quad (31)$$

The resultant continuous, obstacle-free path segment replaces the original points between indices i and j , resulting in a locally refined and feasible trajectory. Fig. 2 visually illustrates the mutation procedure, emphasizing the replacement of inefficient segments with optimized, feasible path segments.

The essence of the A*-guided mutation is to excise locally inefficient segments and replace them with cost-minimal, obstacle-free sub-paths, thereby injecting deterministic improvement rather than purely stochastic perturbation. After two interior control points P_i and P_j have been selected (Algorithm 2), an A* search is executed inside a bounded neighborhood of half-width R centered on the projected

grid cells. Because A* already respects the obstacle mask embedded in the grid, any path returned is feasible by construction. The discrete sequence $\{c_k\}$ is then mapped back to continuous space; horizontal coordinates trace grid centroids, while altitude is interpolated linearly between z_i and z_j . Replacing the original segment $\{P_{i+1}, \dots, P_{j-1}\}$ with these new waypoints yields a chromosome that is simultaneously smoother and shorter (or lower) than before, yet still honours kinematic limits because the climb/descent rate is bounded by the linear interpolation.

In conjunction with the waypoint-connecting crossover, the mutation completes a balanced exploration-exploitation loop. Crossover globally recombines distinct parental topologies, while mutation performs deterministic local refinement inside each individual. Together they maintain population diversity, honour all obstacle and altitude constraints, and continuously push trajectories toward greater efficiency without incurring the computational cost of feasibility repair that plagues generic mutation schemes.

Algorithm 2: A*-Guided Mutation Operator

Input: Parent chromosome \mathbf{P} (set of control points), terrain grid model \mathcal{G} , mutation radius R

Result: Mutated offspring chromosome \mathbf{P}'

- 1 Initialize $\mathbf{P}' \leftarrow \mathbf{P}$;
- 2 Randomly select two interior indices $i, j \in \{2, \dots, N-1\}$ such that $i < j$;
- 3 Set start waypoint $W_{\text{start}} \leftarrow \mathbf{P}(i)$ and goal waypoint $W_{\text{goal}} \leftarrow \mathbf{P}(j)$;
- 4 Map continuous coordinates of W_{start} and W_{goal} to discrete grid cells: $\text{startCell} \leftarrow \text{gridMap}(W_{\text{start}})$, $\text{goalCell} \leftarrow \text{gridMap}(W_{\text{goal}})$;
- 5 Define a localized bounding box around the selected cells:

$$\text{row}_{\min, \max} = [\min(y_{\text{start}}, y_{\text{goal}}) - R, \max(y_{\text{start}}, y_{\text{goal}}) + R]$$

$$\text{col}_{\min, \max} = [\min(x_{\text{start}}, x_{\text{goal}}) - R, \max(x_{\text{start}}, x_{\text{goal}}) + R]$$
- 6 Perform A* search within bounding box from startCell to goalCell;
- 7 **if** No feasible path found **then**
 - 8 | **return** \mathbf{P} (Mutation skipped);
 - 9 **end**
- 10 Convert discrete A* path \mathcal{P} to continuous coordinates via linear altitude interpolation:

$$Z(c_k) = Z(W_{\text{start}}) + \frac{k-1}{|\mathcal{P}| - 1} (Z(W_{\text{goal}}) - Z(W_{\text{start}}))$$
- 11 Replace intermediate control points in \mathbf{P}' between indices i and j with interpolated points from A* path;
- 12 **return** \mathbf{P}' ;

4.3. Dynamic η adaptation for polynomial mutation

Polynomial mutation is widely utilized in multi-objective evolutionary algorithms due to its controlled perturbation characteristics, facilitating a balance between exploration of the solution space and exploitation around promising solutions. However, conventional polynomial mutation operators use a fixed distribution index (η), which often inadequately adapts to the varying demands of different evolutionary stages. To enhance search adaptability and performance, we introduce a dynamic adaptation strategy for the polynomial mutation parameter η , which adjusts mutation intensity systematically across generations.

Polynomial mutation perturbs decision variables according to a polynomial probability distribution defined by the distribution index η . Given a decision variable x_i with bounds $[x_i^{\min}, x_i^{\max}]$, the mutated variable x'_i and the perturbation factor δ_i are given by Eqs. (18) and (19) respectively. Here, A higher η value produces smaller perturbations,

promoting local search (exploitation), while a lower η value generates larger perturbations, enhancing global search (exploration).

To systematically balance exploration and exploitation throughout the evolutionary search, we adopt a dynamic, generation-based adaptive scheme for η . Specifically, the distribution index η is progressively adjusted from lower values (broad mutations) during early generations to higher values (focused, precise mutations) in later evolutionary stages. Formally, we define this dynamic adaptation schedule as follows:

$$\eta(g) = \eta_{\min} + (\eta_{\max} - \eta_{\min}) \left(\frac{g}{g_{\max}} \right)^{\alpha}, \quad (32)$$

where g is the current generation, g_{\max} is the maximum number of generations, and $\alpha \geq 1$ controls the curvature of the transition. In practice, η_{\min} and η_{\max} represent the lower and upper limits of mutation intensity, respectively. A larger α value delays the exploitation phase, allowing more extended exploratory behavior, while a smaller α encourages a quicker transition toward local refinement. Therefore, the distribution index governing polynomial mutation is increased linearly from a near-zero value in the first generation to a high, exploitation-oriented value at the last. At the outset, the resulting heavy-tailed mutation kernel encourages large positional jumps, enabling the algorithm to traverse broad regions of the search space and avoid premature convergence to sub-optimal basins. As generations progress, the steadily rising index progressively narrows the kernel, transforming the same operator into a fine-tuning mechanism that perturbs each coordinate only marginally and thus sharpens convergence on the emerging Pareto front.

Compared with the self-adaptive and feedback-driven schemes surveyed in Section 2, this deterministic schedule offers a favorable complexity-to-benefit ratio. Self-adaptive approaches require additional gene loci to encode control parameters and incur extra genetic operations; feedback methods must maintain online statistics such as success rates or diversity measures, adding bookkeeping overhead. The generation-based schedule, by contrast, is parameter-lean, fully reproducible, and incurs no runtime monitoring cost, yet still captures the essential exploration-to-exploitation transition that underpins effective evolutionary search. The annealed mutation radius also interfaces naturally with the two geometric operators. When the index is low, large perturbations tend to select widely separated waypoint pairs for the A*-guided mutation, prompting the re-planner to discover entirely new corridors and injecting substantial structural diversity. The same broad kernel increases the likelihood that the waypoint-connecting crossover will splice distant interior points, creating novel global route topologies. Later, as the index climbs and the kernel contracts, the A*-guided mutation shifts to a local-repair role, smoothing short detours or altitude spikes without disrupting the overall path, while crossover predominantly recombines already refined sub-routes.

In this way, the generation-controlled polynomial mutation functions as a timing mechanism: it stimulates bold, macroscopic exploration when diversity is most valuable, then recedes into a precise, microscopic adjustment mode as the population converges. By orchestrating its effect with the deterministic, obstacle-aware edits delivered by the A*-based operators, the schedule achieves much of the sophistication of more complex adaptive schemes while retaining transparency, minimal overhead, and straightforward parameterization that are especially advantageous in UAV path planning.

4.4. Integration into MOEA framework

To fully leverage the advantages offered by our specialized waypoint-connecting crossover, A*-guided mutation, and dynamic polynomial mutation operators, these components are integrated seamlessly into a Multi-Objective Evolutionary Algorithm (MOEA) framework. The structured integration strategy ensures cooperative interaction among the customized operators, enhancing their collective efficacy in navigating the complex search landscape of UAV path-planning problems.

Algorithm 3 describes the complete MOEA framework embedding our proposed operators. At each evolutionary generation g , the process begins with parent selection based on Pareto dominance and diversity preservation criteria. The selected parental set undergoes waypoint-connecting crossover (Algorithm 1), strategically recombining solution trajectories while ensuring feasibility via obstacle-aware bridging through A* search. This crossover step actively enriches population diversity, facilitating global exploration of the solution space.

Subsequently, offspring solutions from the crossover undergo refinement using the A*-guided mutation operator (Algorithm 2). This targeted mutation process replaces suboptimal or infeasible path segments, promoting fine-grained exploitation and local optimality. To dynamically balance the exploration-exploitation trade-off throughout the evolutionary process, offspring solutions further undergo polynomial mutation with an adaptively varied distribution index $\eta(g)$. As described earlier, $\eta(g)$ systematically transitions from lower values encouraging exploration at initial generations toward higher values favoring precise exploitation at later stages. Algorithm 3 summarizes this integrated procedure clearly.

Algorithm 3: Integrated MOEA Framework with Problem-specific Operators

Input: Initial population $\mathbf{P}^{(0)}$, maximum generations g_{\max}
Result: Approximate Pareto-optimal solutions

```

1 Initialize  $g \leftarrow 0$ ;
2 while  $g < g_{\max}$  do
3   // Generate offspring via
   // waypoint-connecting crossover (Alg. 1)
4    $\mathbf{C}^{(g)} \leftarrow \text{Crossover}_{A^*}(\mathbf{P}^{(g)}_{\text{selected}})$ ;
5   // Mutate offspring using A*-guided mutation
   // (Alg. 2)
6    $\mathbf{C}^{(g)}_{\text{mutated}} \leftarrow \text{Mutation}_{A^*}(\mathbf{C}^{(g)})$ ;
7   // Apply polynomial mutation with dynamic
   // index  $\eta(g)$ 
8    $\mathbf{C}^{(g)}_{\text{final}} \leftarrow \text{Mutation}_{\eta(g)}(\mathbf{C}^{(g)}_{\text{mutated}})$ ;
9   // Environmental selection (Pareto +
   // diversity)
10   $\mathbf{P}^{(g+1)} \leftarrow \text{EnvironmentalSelection}(\mathbf{P}^{(g)} \cup \mathbf{C}^{(g)}_{\text{final}})$ ;
11   $g \leftarrow g + 1$ ;
12 end
13 return Final Pareto set  $\mathbf{P}^{(g_{\max})}$ ;

```

The integration described in Algorithm 3 provides a cohesive evolutionary mechanism, where domain-specific intelligence embedded into operators significantly improves optimization efficacy. The complementary nature of the waypoint-connecting crossover and A*-guided mutation ensures both broad exploration of promising solution regions and meticulous local optimization. Additionally, the adaptive polynomial mutation dynamically maintains solution diversity and promotes convergence precision across generations, collectively contributing to the robust performance observed in challenging UAV path-planning benchmarks.

5. Experimental study

Recent comprehensive benchmarks of state-of-the-art multi-objective evolutionary algorithms (MOEAs) have shown that the decomposition-based MOEA/D-AWA consistently delivers the strongest performance across a wide spectrum of UAV path-planning scenarios [19]. Its adaptive weight-adjustment mechanism enables robust convergence toward uniformly distributed Pareto fronts while coping effectively with the dynamic, constraint-rich landscapes typical of realistic UAV routing tasks. Consequently, MOEA/D-AWA provides

a well-established and convincing baseline against which to assess the benefit of the heuristic-driven operators and dynamic mutation strategy introduced in the present work. To isolate the contribution of the new operators, we embed them in the MOEA/D-AWA framework without altering any other component. The resulting algorithm referred to as MOEA/D-AWA_{A*+η} integrates (i) an A*-guided waypoint-connecting crossover, (ii) an A*-guided local mutation, and (iii) a generation-dependent polynomial-mutation index $\eta(g)$. All other elements of MOEA/D-AWA, including neighborhood structure, weight updating, and selection strategy, remain unchanged, so any performance differences can be attributed directly to the proposed operators.

The experimental study evaluates eight algorithms representative of the major design paradigms in evolutionary multi-objective optimization. First, NSGA-II/SDR enhances the classic Pareto-based NSGA-II with shift-based density estimation, yielding improved selection pressure on irregularly shaped Pareto fronts [20]. Second, the indicator-based algorithm HypE relies on hypervolume contributions to reward solutions that advance both convergence and diversity simultaneously [21]. A complementary indicator-driven competitor, I_{SDE^+} , employs an advanced diversity metric that remains effective even as the number of objectives grows [22]. From the class of problem-specific methods we include MOEA-2DE, which couples dimension exploration with discrepancy evolution to address the geometric and constraint characteristics inherent to UAV trajectories [6]. To capture recent trends toward learning-assisted evolution, we additionally include two reinforcement-learning-enhanced algorithms. The first, RLM-MDE, integrates multi-strategy differential evolution with Q-learning-based reference-point adaptation to dynamically balance exploration and exploitation while maintaining population diversity across irregular Pareto fronts [51]. The second, DRLOS-EMCMO, augments the multi-objective EMCMO framework with a deep-reinforcement-learning-assisted operator selection mechanism, enabling adaptive choice of variation operators based on population state and constraint feasibility [52]. As the decomposition baseline we retain the original MOEA/D-AWA, whose adaptive weight strategy has proved particularly well-suited to dynamic UAV environments [23]. Finally, the proposed MOEA/D-AWA_{A*+η} variant serves to quantify the gains achievable when A*-guided variation and dynamic mutation are introduced into that strong baseline.

For all experiments, the number of intermediate waypoints defining each UAV trajectory was fixed at seven ($N_{wp} = 7$) across all environments. This configuration follows the benchmark proposed in [19], where the same setting was adopted to balance trajectory flexibility with computational efficiency. Increasing the number of waypoints can improve path smoothness and local adaptability but also enlarges the decision space, thereby increasing computational complexity and convergence time. Maintaining $N_{wp} = 7$ thus ensures a consistent trade-off between precision and efficiency, while enabling direct comparability across studies employing this benchmark.

Within the A*-guided operators, a uniform grid-based representation of the environment was employed for local replanning. The A* search operates over a bounded subgrid $\Omega_{sub} = [r_{min}, r_{max}] \times [c_{min}, c_{max}]$, centered around the start and goal locations and defined by a half-width parameter $R = 20$. This corresponds to a localized search window of approximately 40×40 cells, which provides a balanced trade-off between computational efficiency and spatial resolution for obstacle-aware path refinement. Similar localized grid configurations have been reported in recent UAV path-planning studies, where grid resolution is selected to balance safety margins and computational overhead [53–55]. The same grid resolution and subgrid dimensions were maintained across all experiments to ensure consistency and fair comparison.

For all algorithms, a uniform population size of 20 and a budget of 10,000 function evaluations were assigned per run, and each configuration was executed independently 30 times to ensure statistically robust results. The comparison methods were implemented using their publicly available PlatEMO versions with their recommended default

parameter settings and without any modification, ensuring a fair and consistent baseline.

For the proposed MOEA/D-AWA_{A*+η}, the A*-guided crossover and mutation operators require no additional parameters beyond the localized subgrid search radius ($R = 20$), as described earlier in this section. The polynomial mutation probability was set to $p_m = 1/d$, where $d = 3$ denotes the spatial dimensionality of the UAV trajectory representation. The adaptive mutation distribution index $\eta(g)$ follows Eq. (32) with $\eta_{min} = 1$, $\eta_{max} = 30$, and $\alpha = 1$. This formulation gradually transitions the mutation behavior from exploration to exploitation throughout the evolutionary process.

5.1. Benchmark problems

To thoroughly assess the performance and adaptability of the proposed heuristic-driven evolutionary operators and dynamic polynomial mutation, this study utilizes a comprehensive benchmark suite explicitly designed for multi-objective UAV path planning tasks [19]. This benchmark consists of 14 systematically crafted scenarios grouped into three distinct environment categories—urban, suburban, and mountainous. Each scenario type introduces specific complexities and constraints closely reflecting real-world UAV operational conditions.

The urban scenarios comprise four test cases characterized by densely arranged obstacles simulating metropolitan settings. These scenarios incorporate tightly clustered buildings of varying heights, strict no-fly zones, and pronounced vertical constraints, presenting algorithms with significant spatial navigation challenges. Such problems are essential to validate algorithmic capability in precise maneuvering, collision avoidance, and regulatory adherence in constrained urban airspace. The four suburban scenarios feature environments with moderate obstacle density and smoothly varying terrains. These environments emulate realistic suburban contexts, balancing obstacle avoidance and path efficiency. Suburban scenarios test the algorithms' ability to efficiently navigate moderate complexity landscapes, capturing performance nuances in conditions representative of typical UAV delivery or survey missions. The six mountainous scenarios introduce rigorous challenges through rugged terrains, sharp elevation gradients, and significant altitude variations. These scenarios are particularly effective in evaluating algorithm robustness, adaptability, and capability to manage steep ascents and descents while maintaining optimal path lengths and safe clearances from terrain features.

All test scenarios embed explicit operational constraints—namely the ceiling altitude of the UAV, a mandatory terrain-clearance buffer, and upper bounds on both horizontal and vertical turning angles. These limits guarantee that every synthesized trajectory is flyable and fully consistent with real-world mission requirements. Consequently, the benchmark offers an ideal proving ground for assessing the practical gains afforded by the A*-guided operators and the dynamic mutation scheme proposed in this work. A concise summary of the fourteen environments is given in Table 1. For each case, N_{peaks} (or N_{bldg}) denotes the total number of terrain peaks (or buildings), while their maximum elevation is listed as h_{max}^{peaks} (or h_{max}^{bldg}). If a no-fly zone (NFZ) is present, its altitude ceiling is reported as h_{NFZ} and its center location by the position vector \mathbf{p}_{NFZ} .

5.2. Performance metric

In this study, we evaluate the performance of multi-objective UAV path-planning algorithms using the Hypervolume (HV) metric. Hypervolume is widely recognized in the evolutionary multi-objective optimization community as a robust and comprehensive performance indicator, encapsulating both convergence toward the Pareto front and solution distribution across the objective space. Mathematically, hypervolume represents the volume in objective space dominated by

Table 1

Parameters for the 14 test environments used in the proposed benchmark. Each environment is characterized by distinct attributes such as terrain type, number of peaks or buildings, and no-fly zone specifications, enabling comprehensive evaluations across diverse UAV path-planning scenarios.

Problem name	Environment	Problem ID	$N_{\text{peaks}}/N_{\text{bldg}}$	$h_{\text{max}}^{\text{peaks}}/h_{\text{max}}^{\text{bldg}}$	h_{NFZ}	p_{NFZ}
C01_N100_H450	City	C1	100	450	–	–
C02_N150_H450	City	C2	150	450	–	–
C03_N100_H450_R20_P100,100	City	C3	100	450	20	(100, 100)
C04_N70_H450_R40_P100,100	City	C4	70	450	40	(100, 100)
S01_N120_H40	Suburban	S1	120	40	–	–
S02_N180_H40	Suburban	S2	180	40	–	–
S03_N80_H40_R40_P100,100	Suburban	S3	80	40	40	(100, 100)
S04_N110_H40_R20_P100,100	Suburban	S4	110	40	20	(100, 100)
M01_N100_H300	Mountainous	M1	100	300	–	–
M02_N200_H300	Mountainous	M2	200	300	–	–
M03_N100_H400_R30_P100,100	Mountainous	M3	100	400	30	(100, 100)
M04_N200_H400_R20_P100,100	Mountainous	M4	200	400	20	(100, 100)
M05_N100_H400_R30_P150,150	Mountainous	M5	100	400	30	(150, 150)
M06_N200_H400_R20_P150,150	Mountainous	M6	200	400	20	(150, 150)

the obtained Pareto-optimal set relative to a predetermined reference point. Formally, this can be defined as follows:

$$\text{HV}(P, r) = \text{vol} \left(\bigcup_{x \in P} \{y \in \mathbb{R}^m \mid x \leq y \leq r\} \right), \quad (33)$$

where P denotes the obtained approximation of the Pareto front, m indicates the dimensionality (number of objectives), and r is a chosen reference point in the objective space. A larger HV value reflects superior performance, capturing simultaneously the closeness of the solutions to the true Pareto front (convergence) and their even distribution across the objective space (diversity).

Given these dual characteristics, HV is particularly suitable for assessing algorithm effectiveness in complex UAV trajectory planning tasks, as it provides an integrated measure without necessitating separate diversity metrics. Other diversity-centric metrics, such as spacing or diversity indices alone, tend to isolate distribution quality while neglecting convergence aspects. Such metrics might inadvertently penalize algorithms that exhibit strong convergence properties but slightly narrower distribution, potentially resulting in misleading conclusions [56]. In contrast, the hypervolume metric inherently addresses this shortcoming by simultaneously rewarding both convergence and diversity. The selection of the reference point r was conducted systematically for each benchmark scenario by examining the worst (least desirable) objective values achieved by all algorithms across multiple independent runs. The reference point was set to be strictly dominated by all recorded solution values, thus ensuring consistency with established hypervolume evaluation practices [10,21]. This approach ensures that the hypervolume calculation yields meaningful comparisons by quantifying the dominance space genuinely occupied by the solutions obtained.

Other commonly used metrics, such as the Inverted Generational Distance (IGD), were considered but found unsuitable for our purposes. IGD measures the average Euclidean distance from a known true Pareto front to solutions produced by an algorithm, effectively capturing both convergence and diversity. However, computing IGD requires explicit knowledge of the exact Pareto front, typically only available for synthetic benchmarks or mathematically tractable problems [57]. Since the present work utilizes realistic UAV path-planning benchmarks where precise Pareto-optimal solutions are unknown, IGD is inapplicable, further justifying our reliance on hypervolume as the performance metric.

6. Results and discussions

This section consolidates and analyzes the empirical findings obtained on the fourteen-problem UAV path-planning benchmark. We begin by presenting an aggregate hypervolume comparison against state-of-the-art baselines, followed by a convergence analysis that highlights the speed and stability of the proposed method. Next, we dissect

the contribution of each problem-specific operator A*-guided crossover, A*-guided mutation, and the adaptive polynomial-mutation index both in isolation and in combination, clarifying how they synergistically improve search performance. A dedicated ablation study then contrasts dynamic versus fixed values of the mutation index η , demonstrating the consistent advantage of the generation-dependent schedule. Finally, representative trajectory visualizations are provided to give qualitative insight into the feasibility and efficiency of the paths produced.

For completeness, the supplementary material includes: (i) full convergence curves for all fourteen test problems, (ii) extended operator-level statistics, (iii) the complete η -ablation box-plot suite, and (iv) additional path visualizations for each benchmark environment.

6.1. Overall performance analysis

The results summarized in Table 2 demonstrate the comparative hypervolume performance of the proposed MOEA/D-AWA with the integrated A*-guided operators and adaptive polynomial mutation index (MOEA/D-AWA_{A*+ η}) against seven prominent evolutionary multi-objective optimization algorithms across fourteen benchmark UAV path-planning scenarios. The hypervolume metric offers a clear and comprehensive indication of overall solution quality by measuring the volume of the objective space dominated by the approximated Pareto front; thus, higher hypervolume values directly correspond to superior convergence and diversity (reference point selection described in Section 5.2). Examining the results presented in Table 2, MOEA/D-AWA_{A*+ η} consistently outperformed all competing algorithms—NSGA-II/SDR, HypE, I_{SDE+} , MOEA-2DE, MOEA/D-AWA, DRLOS-EMCMO, and RLMMDE across every tested scenario. The superior performance of MOEA/D-AWA_{A*+ η} is not only statistically evident through its highest mean hypervolume scores but also substantiated by the Wilcoxon signed-rank test at a significance level of $\alpha = 0.05$. The uniformly favorable indicators (\blacktriangle) observed for all fourteen benchmark problems confirm that the improvements achieved by the proposed method are statistically significant and consistent across problem classes. In contrast, none of the comparative algorithms achieved statistical equivalence (\blacklozenge) or superiority (\blacktriangle) in any benchmark instance, while their performance was predominantly characterized by statistically inferior outcomes (\blacktriangledown). The inclusion of the two reinforcement-learning-enhanced algorithms, DRLOS-EMCMO and RLMMDE, provides an additional comparative perspective on learning-based adaptive strategies within multi-objective optimization. DRLOS-EMCMO, which employs deep reinforcement learning to adaptively select evolutionary operators based on population state and constraint feasibility, demonstrated reasonable competitiveness across several benchmarks but did not attain superiority in any case. Similarly, RLMMDE, which integrates multi-strategy differential evolution with a Q-learning-based reference-point adaptation mechanism, exhibited adaptive exploration-exploitation balancing yet remained notably below the proposed approach in terms of both convergence and stability. Their overall lower

Table 2

Hypervolume (mean \pm std) for the fourteen benchmark problems. Triangle-up (\blacktriangle) = significantly better; diamond (\lozenge) = statistically equal; triangle-down (\blacktriangledown) = significantly worse, according to Wilcoxon signed-rank tests versus the best algorithm in each row. Best mean values are in **bold**.

Problem	NSGA-II/SDR	HypE	I_{SDE+}	MOEA-2DE	MOEA/D-AWA	DRLOS-EMCMO	RIMMDE	MOEA/D-AWA $_{A^*+\eta}$
C1	8.8097e-01 \pm 7.13e-03 \blacktriangledown	8.8037e-01 \pm 7.04e-03 \blacktriangledown	8.7640e-01 \pm 9.56e-03 \blacktriangledown	8.5616e-01 \pm 1.28e-02 \blacktriangledown	8.9433e-01 \pm 1.17e-02 \blacktriangledown	8.6002e-01 \pm 1.65e-02 \blacktriangledown	7.9349e-01 \pm 1.97e-02 \blacktriangledown	9.1201e-01 \pm 1.45e-03 \blacktriangle
C2	8.4843e-01 \pm 1.60e-02 \blacktriangledown	8.4894e-01 \pm 1.80e-02 \blacktriangledown	8.3926e-01 \pm 1.09e-02 \blacktriangledown	8.1911e-01 \pm 1.35e-02 \blacktriangledown	8.8689e-01 \pm 1.69e-02 \blacktriangledown	8.1576e-01 \pm 1.76e-02 \blacktriangledown	8.0884e-01 \pm 1.41e-02 \blacktriangledown	9.1129e-01 \pm 1.59e-03 \blacktriangle
C3	8.8054e-01 \pm 1.64e-02 \blacktriangledown	8.8363e-01 \pm 1.26e-02 \blacktriangledown	8.7523e-01 \pm 1.71e-02 \blacktriangledown	8.4747e-01 \pm 1.20e-02 \blacktriangledown	8.8868e-01 \pm 9.06e-03 \blacktriangledown	8.4870e-01 \pm 2.56e-02 \blacktriangledown	7.9323e-01 \pm 7.04e-02 \blacktriangledown	9.0989e-01 \pm 3.02e-03 \blacktriangle
C4	8.7348e-01 \pm 2.01e-02 \blacktriangledown	8.6553e-01 \pm 1.48e-02 \blacktriangledown	8.5929e-01 \pm 1.65e-02 \blacktriangledown	8.4056e-01 \pm 1.10e-02 \blacktriangledown	8.9693e-01 \pm 6.12e-03 \blacktriangledown	8.5845e-01 \pm 2.74e-02 \blacktriangledown	7.8725e-01 \pm 2.79e-02 \blacktriangledown	9.1050e-01 \pm 2.15e-03 \blacktriangle
S1	9.2630e-01 \pm 1.82e-03 \blacktriangledown	9.2633e-01 \pm 1.53e-03 \blacktriangledown	9.2607e-01 \pm 2.04e-03 \blacktriangledown	9.2442e-01 \pm 8.73e-04 \blacktriangledown	9.2731e-01 \pm 2.58e-03 \blacktriangledown	9.2132e-01 \pm 2.01e-03 \blacktriangledown	9.1941e-01 \pm 1.38e-03 \blacktriangledown	9.3075e-01 \pm 8.35e-04 \blacktriangle
S2	9.2169e-01 \pm 3.46e-03 \blacktriangledown	9.2019e-01 \pm 1.43e-03 \blacktriangledown	9.1971e-01 \pm 1.54e-03 \blacktriangledown	9.1803e-01 \pm 108e-03 \blacktriangledown	9.2799e-01 \pm 4.38e-03 \blacktriangledown	9.1757e-01 \pm 3.14e-03 \blacktriangledown	9.1406e-01 \pm 1.21e-03 \blacktriangledown	9.3187e-01 \pm 1.25e-03 \blacktriangle
S3	9.2231e-01 \pm 1.25e-03 \blacktriangledown	9.2201e-01 \pm 1.29e-03 \blacktriangledown	9.2176e-01 \pm 1.48e-03 \blacktriangledown	9.2021e-01 \pm 1.18e-03 \blacktriangledown	9.2086e-01 \pm 2.77e-03 \blacktriangledown	9.1683e-01 \pm 9.01e-04 \blacktriangledown	9.1071e-01 \pm 8.49e-04 \blacktriangledown	9.3013e-01 \pm 2.73e-03 \blacktriangle
S4	9.2373e-01 \pm 1.76e-03 \blacktriangledown	9.2393e-01 \pm 1.31e-03 \blacktriangledown	9.2246e-01 \pm 1.55e-03 \blacktriangledown	9.2167e-01 \pm 1.05e-03 \blacktriangledown	9.2268e-01 \pm 3.31e-03 \blacktriangledown	9.1791e-01 \pm 1.64e-03 \blacktriangledown	9.1521e-01 \pm 1.57e-03 \blacktriangledown	9.3152e-01 \pm 2.21e-03 \blacktriangle
M1	8.6999e-01 \pm 2.75e-02 \blacktriangledown	8.6280e-01 \pm 2.26e-02 \blacktriangledown	8.5585e-01 \pm 1.35e-02 \blacktriangledown	8.6142e-01 \pm 1.87e-02 \blacktriangledown	9.2493e-01 \pm 5.04e-03 \blacktriangledown	8.4782e-01 \pm 2.21e-02 \blacktriangledown	8.1826e-01 \pm 2.14e-02 \blacktriangledown	9.3037e-01 \pm 2.72e-03 \blacktriangle
M2	8.5233e-01 \pm 1.47e-02 \blacktriangledown	8.4917e-01 \pm 2.07e-03 \blacktriangledown	8.4990e-01 \pm 1.04e-02 \blacktriangledown	8.8427e-01 \pm 1.11e-02 \blacktriangledown	9.2685e-01 \pm 7.60e-03 \blacktriangledown	8.4520e-01 \pm 1.62e-03 \blacktriangledown	8.3603e-01 \pm 2.82e-03 \blacktriangledown	9.3211e-01 \pm 8.58e-04 \blacktriangle
M3	8.8839e-01 \pm 2.68e-02 \blacktriangledown	8.7602e-01 \pm 2.47e-02 \blacktriangledown	8.6160e-01 \pm 2.46e-02 \blacktriangledown	8.7511e-01 \pm 6.56e-03 \blacktriangledown	9.2113e-01 \pm 9.33e-03 \blacktriangledown	8.8678e-01 \pm 2.40e-02 \blacktriangledown	8.3174e-01 \pm 7.30e-02 \blacktriangledown	9.3104e-01 \pm 1.20e-03 \blacktriangle
M4	8.2882e-01 \pm 2.56e-02 \blacktriangledown	8.2565e-01 \pm 2.76e-02 \blacktriangledown	8.1198e-01 \pm 2.33e-02 \blacktriangledown	8.1254e-01 \pm 1.94e-02 \blacktriangledown	9.1766e-01 \pm 1.50e-02 \blacktriangledown	8.1651e-01 \pm 2.65e-02 \blacktriangledown	7.9699e-01 \pm 3.58e-02 \blacktriangledown	9.3176e-01 \pm 1.43e-03 \blacktriangle
M5	8.5928e-01 \pm 1.15e-02 \blacktriangledown	8.5472e-01 \pm 1.08e-02 \blacktriangledown	8.4965e-01 \pm 1.11e-02 \blacktriangledown	8.4869e-01 \pm 6.28e-03 \blacktriangledown	9.1023e-01 \pm 1.87e-02 \blacktriangledown	8.5402e-01 \pm 2.25e-02 \blacktriangledown	7.9008e-01 \pm 6.71e-02 \blacktriangledown	9.3026e-01 \pm 2.61e-03 \blacktriangle
M6	8.3709e-01 \pm 4.35e-02 \blacktriangledown	8.1940e-01 \pm 3.84e-02 \blacktriangledown	8.0390e-01 \pm 2.05e-02 \blacktriangledown	8.2364e-01 \pm 1.51e-02 \blacktriangledown	9.1594e-01 \pm 2.04e-02 \blacktriangledown	8.1543e-01 \pm 3.84e-02 \blacktriangledown	7.9321e-01 \pm 8.12e-02 \blacktriangledown	9.2902e-01 \pm 4.91e-03 \blacktriangle

Table 3

Comparison of path length and path height between MOEA/D-AWA and MOEA/D-AWA $_{A^*+\eta}$ across representative benchmark problems. Bold values indicate better performance. Percentage improvement is calculated relative to MOEA/D-AWA.

Problem	Path length (L) ↓			Path height (H_{avg}) ↓		
	MOEA/D-AWA	MOEA/D-AWA $_{A^*+\eta}$	Improvement (%)	MOEA/D-AWA	MOEA/D-AWA $_{A^*+\eta}$	Improvement (%)
C1	436.99	313.35	28.2	133.90	90.79	32.1
C2	574.66	303.28	47.2	198.39	91.14	54.0
S3	388.88	310.98	20.0	33.63	19.91	40.7
M4	661.29	389.94	41.0	194.61	30.71	84.2
M5	545.39	339.43	37.7	146.38	31.67	78.3

Table 4

Hypervolume (mean \pm std) achieved by MOEA/D-AWA when augmented with the A*-guided crossover (X), A*-guided mutation (M), and adaptive polynomial mutation (η) operators — both individually and in all possible combinations — across the fourteen benchmark problems. Triangle-up (\blacktriangle) = significantly better; diamond (\lozenge) = statistically equal; triangle-down (\blacktriangledown) = significantly worse, according to Wilcoxon signed-rank tests versus the best variant in each row. Best mean values are in **bold**.

Problem	MOEA/D-AWA (base)	MOEA/D-AWA $_{A^*+X}$	MOEA/D-AWA $_{A^*+M}$	MOEA/D-AWA $_{\eta,adapt}$	MOEA/D-AWA $_{A^*+X+M}$	MOEA/D-AWA $_{A^*+\eta}$	MOEA/D-AWA $_{A^*+\eta+g}$	MOEA/D-AWA $_{A^*+\eta+g+X}$
C1	8.9434e-01 \pm 1.17e-02 \blacktriangledown	8.9659e-01 \pm 7.559e-03 \blacktriangledown	8.0178e-01 \pm 1.691e-02 \blacktriangledown	9.0180e-01 \pm 6.849e-03 \blacktriangledown	7.9149e-01 \pm 1.014e-02 \blacktriangledown	9.1161e-01 \pm 9.389e-04 \blacktriangledown	9.0746e-01 \pm 4.023e-03 \blacktriangledown	9.1201e-01 \pm 1.453e-03 \blacktriangle
C2	8.8689e-01 \pm 1.694e-02 \blacktriangledown	8.7847e-01 \pm 2.318e-02 \blacktriangledown	7.8837e-01 \pm 1.264e-02 \blacktriangledown	8.9097e-01 \pm 1.512e-02 \blacktriangledown	7.8166e-01 \pm 1.401e-02 \blacktriangledown	9.1081e-01 \pm 2.229e-03 \blacktriangledown	9.0008e-01 \pm 1.376e-02 \blacktriangledown	9.1129e-01 \pm 1.594e-03 \blacktriangle
C3	8.8869e-01 \pm 9.063e-03 \blacktriangledown	9.0453e-01 \pm 5.273e-03 \blacktriangledown	8.1384e-01 \pm 2.156e-02 \blacktriangledown	8.9148e-01 \pm 9.381e-03 \blacktriangledown	7.1313e-01 \pm 6.431e-03 \blacktriangledown	9.0967e-01 \pm 3.046e-03 \blacktriangledown	8.8980e-01 \pm 7.481e-03 \blacktriangledown	9.0990e-01 \pm 3.120e-03 \blacktriangle
C4	8.9693e-01 \pm 6.130e-03 \blacktriangledown	9.0323e-01 \pm 5.103e-03 \blacktriangledown	7.9779e-01 \pm 1.761e-02 \blacktriangledown	9.0149e-01 \pm 6.365e-03 \blacktriangledown	7.5925e-01 \pm 3.143e-02 \blacktriangledown	9.1022e-01 \pm 2.087e-03 \blacktriangledown	9.0686e-01 \pm 5.228e-03 \blacktriangledown	9.1051e-01 \pm 2.152e-03 \blacktriangle
S1	9.2732e-01 \pm 2.589e-03 \blacktriangledown	9.2909e-01 \pm 8.114e-04 \blacktriangledown	9.2074e-01 \pm 7.909e-04 \blacktriangledown	9.2918e-01 \pm 2.377e-03 \blacktriangledown	9.2162e-01 \pm 9.098e-04 \blacktriangledown	9.3064e-01 \pm 1.090e-03 \blacktriangledown	9.2933e-01 \pm 2.395e-03 \blacktriangledown	9.3075e-01 \pm 8.357e-04 \blacktriangle
S2	9.2799e-01 \pm 4.389e-03 \blacktriangledown	9.2619e-01 \pm 2.823e-03 \blacktriangledown	9.1407e-01 \pm 1.936e-03 \blacktriangledown	9.2939e-01 \pm 4.001e-03 \blacktriangledown	9.1721e-01 \pm 1.554e-03 \blacktriangledown	9.3148e-01 \pm 1.598e-03 \blacktriangledown	9.3066e-01 \pm 3.213e-03 \blacktriangledown	9.3188e-01 \pm 1.256e-03 \blacktriangle
S3	9.2087e-01 \pm 2.771e-03 \blacktriangledown	9.2435e-01 \pm 3.566e-03 \blacktriangledown	9.1843e-01 \pm 1.116e-03 \blacktriangledown	9.2377e-01 \pm 4.370e-03 \blacktriangledown	9.1541e-01 \pm 1.612e-03 \blacktriangledown	9.2824e-01 \pm 3.222e-03 \blacktriangledown	9.3497e-01 \pm 3.452e-03 \blacktriangledown	9.3014e-01 \pm 2.733e-03 \blacktriangle
S4	9.2269e-01 \pm 3.318e-03 \blacktriangledown	9.2715e-01 \pm 2.772e-03 \blacktriangledown	9.1918e-01 \pm 9.673e-04 \blacktriangledown	9.2520e-01 \pm 2.977e-03 \blacktriangledown	9.1950e-01 \pm 1.770e-03 \blacktriangledown	9.3127e-01 \pm 2.856e-03 \blacktriangledown	9.2952e-01 \pm 3.925e-03 \blacktriangledown	9.3152e-01 \pm 2.213e-03 \blacktriangle
M1	9.2493e-01 \pm 5.047e-03 \blacktriangledown	9.2252e-01 \pm 3.009e-02 \blacktriangledown	8.2379e-01 \pm 3.911e-02 \blacktriangledown	9.2341e-01 \pm 7.292e-03 \blacktriangledown	8.2141e-01 \pm 6.226e-03 \blacktriangledown	9.2854e-01 \pm 4.225e-03 \blacktriangledown	9.3037e-01 \pm 2.722e-03 \blacktriangledown	9.3037e-01 \pm 2.722e-03 \blacktriangle
M2	9.2685e-01 \pm 7.601e-03 \blacktriangledown	8.8121e-01 \pm 2.159e-02 \blacktriangledown	8.3686e-01 \pm 2.601e-03 \blacktriangledown	9.2422e-01 \pm 8.646e-03 \blacktriangledown	8.5060e-01 \pm 4.562e-03 \blacktriangledown	9.3121e-01 \pm 3.132e-03 \blacktriangledown	9.2941e-01 \pm 6.196e-03 \blacktriangledown	9.3211e-01 \pm 8.582e-04 \blacktriangle
M3	9.2114e-01 \pm 9.335e-03 \blacktriangledown	9.2027e-01 \pm 1.264e-02 \blacktriangledown	8.2952e-01 \pm 2.078e-02 \blacktriangledown	9.2538e-01 \pm 7.488e-03 \blacktriangledown	7.3477e-01 \pm 6.397e-03 \blacktriangledown	9.3061e-01 \pm 1.642e-03 \blacktriangledown	9.2613e-01 \pm 8.275e-03 \blacktriangledown	9.3105e-01 \pm 1.207e-03 \blacktriangle
M4	9.1766e-01 \pm 1.501e-02 \blacktriangledown	8.5321e-01 \pm 2.712e-02 \blacktriangledown	7.9862e-01 \pm 8.326e-03 \blacktriangledown	9.1902e-01 \pm 1.064e-02 \blacktriangledown	7.7694e-01 \pm 2.753e-02 \blacktriangledown	9.3164e-01 \pm 1.509e-03 \blacktriangledown	9.2695e-01 \pm 8.428e-03 \blacktriangledown	9.3177e-01 \pm 1.433e-03 \blacktriangle
M5	9.1023e-01 \pm 1.879e-02 \blacktriangledown	9.0166e-01 \pm 2.063e-02 \blacktriangledown	8.1116e-01 \pm 2.790e-02 \blacktriangledown	9.2188e-01 \pm 1.182e-02 \blacktriangled				

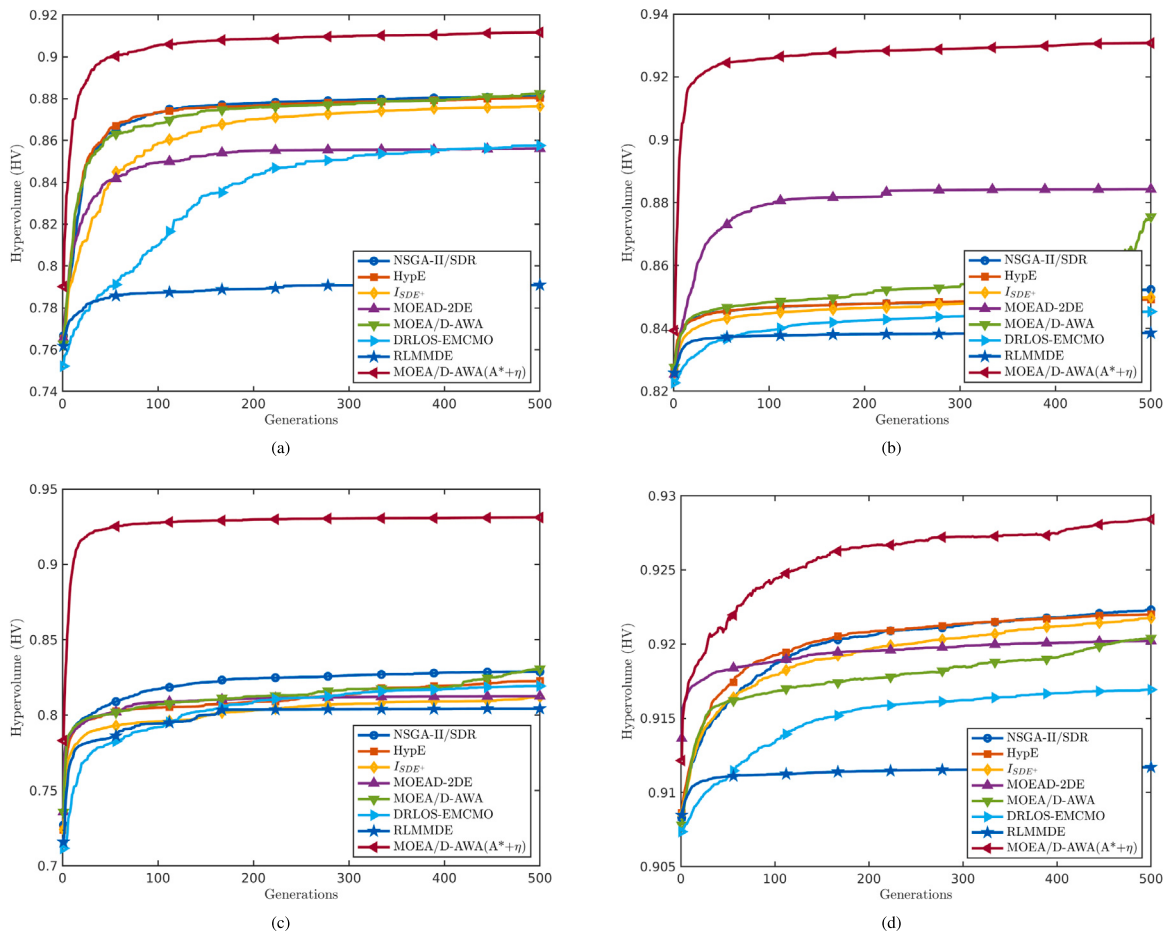


Fig. 3. Convergence characteristics of the compared algorithms in representative benchmark environments: (a) Urban environment C1 featuring 100 buildings without NFZ, (b) Mountainous environment M2 characterized by dense, high-altitude peaks without NFZ, (c) Mountainous environment M4 with dense peaks and a compact NFZ, and (d) Suburban environment S3 characterized by rolling terrain and scattered buildings with a large NFZ. These plots illustrate the convergence efficiency and solution quality of the proposed MOEA/D-AWA_{A^{*}+η} against other benchmarked algorithms.

refinement around high-quality regions of the Pareto front. This self-regulating behavior ensures both comprehensive search coverage and fine-grained exploitation in later generations.

Finally, it is noteworthy that, while algorithms such as MOEA-2DE, I_{SDE}^+ , and DRLOS-EMCMO occasionally exhibited modest improvements in individual problems, their standard deviations were relatively large, indicating higher variability and instability. In contrast, MOEA/D-AWA_{A^{*}+η} consistently yielded smaller standard deviations, reflecting its robust and reliable performance across all fourteen environments. This stability is of particular importance in real-world UAV path-planning applications, where predictable performance and consistent convergence behavior are critical for mission safety and operational reliability. Overall, the results confirm that the synergistic combination of A^{*}-guided evolutionary variation and adaptive mutation control provides a decisive advantage over both classical and learning-based multi-objective algorithms.

6.2. Convergence analysis

Building upon the superior hypervolume performance observed earlier, we now analyze the convergence characteristics of the algorithms across representative benchmark scenarios. Fig. 3 presents comparative convergence curves of hypervolume progression, offering clear insights into the optimization dynamics and stability of each algorithm.

In the urban environment C1, characterized by a dense distribution of buildings without any explicit No-Fly Zones (NFZs), MOEA/D-AWA_{A^{*}+η} exhibits rapid ascent toward superior hypervolume levels,

achieving both swift and stable convergence. As shown in Fig. 3(a), the algorithm effectively exploits domain-specific heuristic knowledge encoded within the A^{*}-guided operators and the adaptive polynomial mutation mechanism, facilitating efficient exploration and exploitation of promising regions. In contrast, NSGA-II/SDR, HypE, and MOEA-2DE converge at a notably slower pace and stagnate at lower hypervolume values due to their limited capacity to navigate dense urban structures. The reinforcement-learning-based competitors, DRLOS-EMCMO and RLMMDE, show moderate early improvements owing to adaptive operator selection and reference-point adjustment but stabilize prematurely, highlighting that general learning-based adaptation lacks the domain awareness embedded in the proposed approach.

In the mountainous environment M2 (Fig. 3(b)), characterized by steep elevation changes and high-altitude peaks, similar convergence patterns are observed. MOEA/D-AWA_{A^{*}+η} rapidly approaches near-optimal hypervolume values within the early generations and maintains steady incremental gains thereafter, reflecting a robust balance between exploration and exploitation. DRLOS-EMCMO displays improved responsiveness in the initial search phases but lacks consistent refinement under complex terrain, while RLMMDE, though stable, adapts poorly to abrupt topographical variations. The other algorithms exhibit slower hypervolume growth and lower asymptotic performance, underscoring their limited adaptability in rugged landscapes.

Increasing the complexity further, the mountainous environment M4 (Fig. 3(c)) introduces a compact NFZ that restricts feasible search space. MOEA/D-AWA_{A^{*}+η} effectively mitigates these constraints through its embedded A^{*}-based spatial heuristics, enabling precise

navigation around obstacles and ensuring rapid, feasible trajectory generation. This spatial awareness results in early divergence from competing algorithms, confirming its superior constraint-handling efficiency. DRLOS-EMCMO benefits slightly from operator adaptivity but fails to sustain refinement, while RLMMDE and traditional methods like NSGA-II/SDR and MOEA/D-AWA exhibit shallow convergence trends, often trapped in suboptimal basins due to the absence of explicit constraint-aware variation.

Finally, in the suburban environment S3 (Fig. 3(d)), characterized by rolling terrain, scattered buildings, and an extensive NFZ, MOEA/D-AWA_{A*+η} maintains consistent improvement across generations, achieving smooth and stable convergence with minimal fluctuation. Its combination of adaptive mutation control and heuristic-guided variation ensures efficient adaptation to environmental heterogeneity. DRLOS-EMCMO achieves slightly better mid-phase performance than other baselines but fails to sustain progress toward the end of evolution, while RLMMDE converges steadily yet more slowly due to weaker sensitivity to spatial constraints. In contrast, algorithms such as HypE and I_{SDE^+} stagnate early and achieve lower hypervolume gains. Collectively, these convergence analyses reinforce the earlier hypervolume findings and further emphasize the robustness of MOEA/D-AWA_{A*+η}. By coupling domain-informed A*-guided operators with adaptive mutation modulation, the algorithm achieves rapid, stable, and consistent convergence across diverse conditions. While reinforcement-learning-based frameworks like DRLOS-EMCMO and RLMMDE introduce valuable self-adaptive behaviors, their generalized learning paradigms remain less effective for spatially constrained UAV path-planning tasks where explicit environmental awareness is crucial. Overall, MOEA/D-AWA_{A*+η} demonstrates the fastest and most stable convergence behavior, affirming its adaptability and reliability for real-world UAV trajectory optimization.

6.3. Contribution of individual and combined operators

To further investigate the reasons behind the superior performance of MOEA/D-AWA_{A*+η} demonstrated previously, we now examine the individual and combined contributions of the A*-guided crossover (X), A*-guided mutation (M), and adaptive polynomial mutation (η) operators, as summarized in Table 4. This ablation analysis allows us to quantify the isolated effect of each operator, in addition to understanding how their interactions shape overall optimization performance.

Across the fourteen benchmark problems, the baseline MOEA/D-AWA achieves an average hypervolume of 0.9130. Incorporating the A*-guided crossover alone (MOEA/D-AWA_{A*-X}) yields a mean of 0.9020, corresponding to a slight degradation of 0.0110. While this variant occasionally provides improvements in specific cases (e.g., C3 and C4), the aggregate numbers indicate that crossover by itself does not consistently enhance performance. Its qualitative role, however, remains important: by connecting feasible waypoints into coherent segments, crossover provides structural guidance that becomes more valuable when paired with adaptive mechanisms. The A*-guided mutation operator on its own (MOEA/D-AWA_{A*-M}) performs considerably worse. Its mean hypervolume drops to 0.8397, a reduction of 0.0733 compared to the baseline, with especially sharp declines in complex environments such as C2, C4, and M3–M5. This confirms that while heuristic mutation injects local refinements, its limited exploration capability causes rapid stagnation and loss of diversity, leading to overall poor outcomes when applied in isolation. In contrast, the adaptive polynomial mutation (η -adapt) achieves a small but consistent positive effect. With an average hypervolume of 0.9164, it improves upon the baseline by 0.0033, while also reducing variance across most problems (e.g., 0.0068 on C1 versus 0.0117 for the base). This reflects the mechanism's strength: dynamically adjusting mutation strength maintains exploration in early generations and transitions smoothly to exploitation later, thereby stabilizing convergence. Even though the

absolute gain is modest, the consistent trend across all fourteen scenarios demonstrates the robustness of adaptive mutation as a standalone operator.

When operators are combined, their complementarity becomes apparent. Pairing A*-guided crossover with adaptive mutation (MOEA/D-AWA_{A*-X+η}) yields a mean hypervolume of 0.9248, corresponding to an improvement of 0.0118 over the baseline and nearly double the benefit of η alone. For example, on problem M4, the base algorithm records 0.918, while A*-X+ η climbs to 0.932, showing how crossover's feasibility-preserving recombination synergizes with the adaptive fine-tuning of polynomial mutation to achieve consistently better outcomes. Similarly, combining A*-guided mutation with adaptive mutation (MOEA/D-AWA_{A*-M+η}) substantially recovers the deficit of mutation alone. The mean rises to 0.9206, representing an improvement of 0.0075 over the baseline and a striking turnaround from the 0.0733 deficit of A*-M. In several suburban and mountainous scenarios (e.g., S1, S2, M1–M6), this variant achieves statistical equivalence with the best-performing configuration, indicating that adaptive mutation can effectively channel heuristic refinements into productive local search when the two operators are coupled.

Finally, integrating all three operators (MOEA/D-AWA_{A*+η}) produces the strongest and most consistent results. The mean hypervolume increases to 0.9252, a gain of 0.0122 over the baseline and the highest among all ablation variants. More importantly, this configuration achieves statistically significant superiority in all fourteen problems, with no ties or degradations. The improvements are particularly visible in the mountainous problems (M3–M6), where the base algorithm averages around 0.915 but the full operator set consistently exceeds 0.930. These results highlight how the combined interplay of crossover (global feasibility maintenance), mutation (local refinement), and adaptive mutation (dynamic control of search intensity) delivers a balanced and highly effective optimization process.

Taken together, the quantitative evidence and qualitative insights converge on the same conclusion: while adaptive mutation provides the only consistent isolated benefit, and while crossover or mutation alone are insufficient. Their integration, particularly under adaptive control produces a synergistic effect that consistently drives convergence toward higher-quality and more robust solutions across all benchmark environments.

6.4. Analysis of dynamic polynomial mutation index (η)

Building upon the insights gained from operator contributions, we further explore the critical role played by the polynomial mutation index (η) through an extensive ablation study, as depicted in Fig. 4. This analysis compares the performance of fixed polynomial mutation indices ($\eta = \{5, 10, 15, 20, 25, 30\}$) against the proposed adaptive η approach in representative benchmark environments, including urban (C1), mountainous (M2 and M6), and suburban (S3) scenarios. As previously discussed in Section 4.3, the adaptive approach employs Eq. (32) for dynamic control of η , where we set $\eta_{\min} = 1$, $\eta_{\max} = 30$, and the sensitivity parameter $\alpha = 1$ for all experimental implementations. These values were selected to provide a wide yet controlled range for mutation intensity, effectively balancing exploration and exploitation during the evolutionary optimization process.

Observing the results from Fig. 4(a) (urban environment C1), we see that lower constant values of η (e.g., $\eta = 5$ and $\eta = 10$) yield moderately competitive performance, likely due to their higher mutation intensity facilitating broader exploration of the search space. Conversely, excessively high η values (e.g., $\eta = 25$ and $\eta = 30$) consistently underperform, indicating overly restrictive mutations that stifle necessary population diversity. The adaptive η approach notably delivers significantly improved hypervolume performance, surpassing all fixed settings due to its ability to dynamically balance exploration and exploitation throughout the evolutionary run.

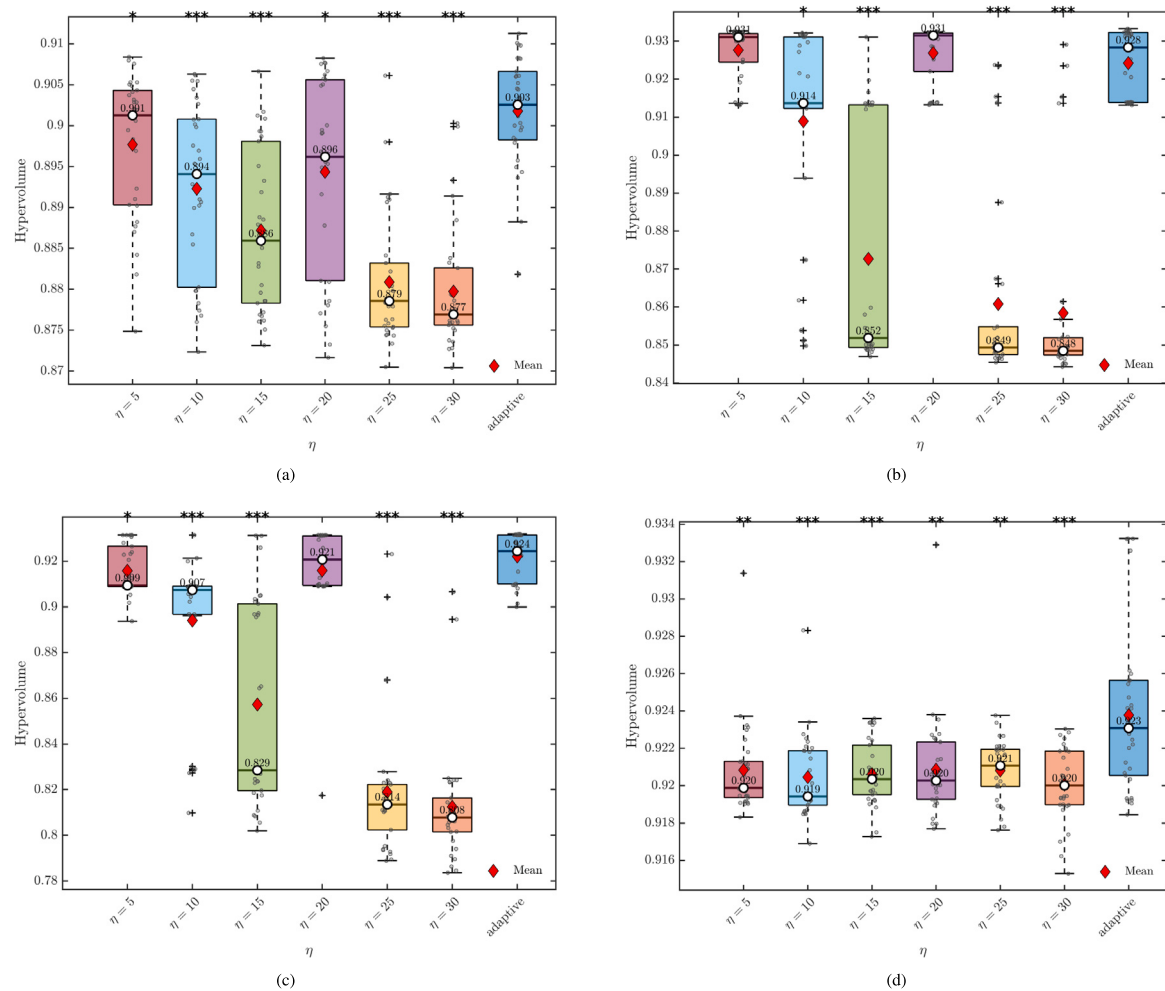


Fig. 4. Ablation study evaluating the impact of different constant values of the polynomial mutation index (η) compared to the proposed adaptive η strategy across selected benchmark problems: (a) Urban environment C1, (b) Mountainous environment M2, (c) Mountainous environment M6, and (d) Suburban environment S3. The results clearly demonstrate that the adaptive approach provides consistently superior or competitive hypervolume performance, underscoring its effectiveness in dynamically adjusting mutation intensity throughout the evolutionary process.

Similar patterns are evident in the mountainous environment M2 (Fig. 4(b)). Here, the adaptive strategy substantially outperforms the fixed η indices, demonstrating a pronounced advantage in managing mutation intensity adaptively within a more complex, rugged search landscape. Specifically, the fixed $\eta = 15$ scenario demonstrates particularly poor performance, underscoring the risk associated with an arbitrarily chosen intermediate mutation intensity that neither effectively explores nor sufficiently exploits local optima. By continuously adapting, the proposed approach intelligently shifts mutation intensity, significantly outperforming static alternatives and indicating its robustness in handling challenging terrains. The analysis of mountainous environment M6 (Fig. 4(c)) further reinforces these findings. This environment, characterized by complex peak distributions and challenging constraints, clearly favors the adaptive approach. Although certain fixed η values (such as $\eta = 5$) occasionally yield reasonable results due to aggressive exploration, these solutions lack stability and show significant variance. Conversely, higher η values again result in suboptimal performance. In contrast, the adaptive η consistently strikes an optimal balance between exploration depth and solution precision, as evidenced by its superior hypervolume results and comparatively lower variance.

Finally, the suburban scenario S3 (Fig. 4(d)) presents an environment where performance distinctions among fixed η values are narrower, suggesting a less sensitive response to mutation intensity

within relatively simpler landscapes. Nonetheless, the adaptive η continues to demonstrate clear advantages by consistently achieving top-tier median and mean hypervolume scores. Its adaptive nature permits tailored mutation intensity across evolutionary stages, preserving necessary population diversity during early generations and progressively intensifying exploitation during later phases. Consequently, it surpasses fixed-index scenarios that inevitably encounter suboptimal trade-offs between exploration and exploitation. This firmly establishes the effectiveness of the proposed adaptive polynomial mutation strategy compared to the fixed setting, wherein the adaptive η dynamically responds to evolving population characteristics and problem-specific complexities, providing an optimal mutation balance throughout the entire evolutionary process.

6.5. Trajectory visualization

Fig. 5 illustrates representative UAV trajectories obtained using MOEA/D-AWA $_{A^*+\eta}$ in comparison to the other benchmarked algorithms, across distinct environmental conditions. These visualizations corroborate the quantitative findings presented in the earlier sections by offering qualitative insights into the practical trajectory behavior and constraint-handling capability of each algorithm. In the urban environment (C2, Fig. 5(a)), characterized by densely distributed, high-rise structures without explicit no-fly zones (NFZs), MOEA/D-AWA $_{A^*+\eta}$ demonstrates a clear ability to navigate efficiently through

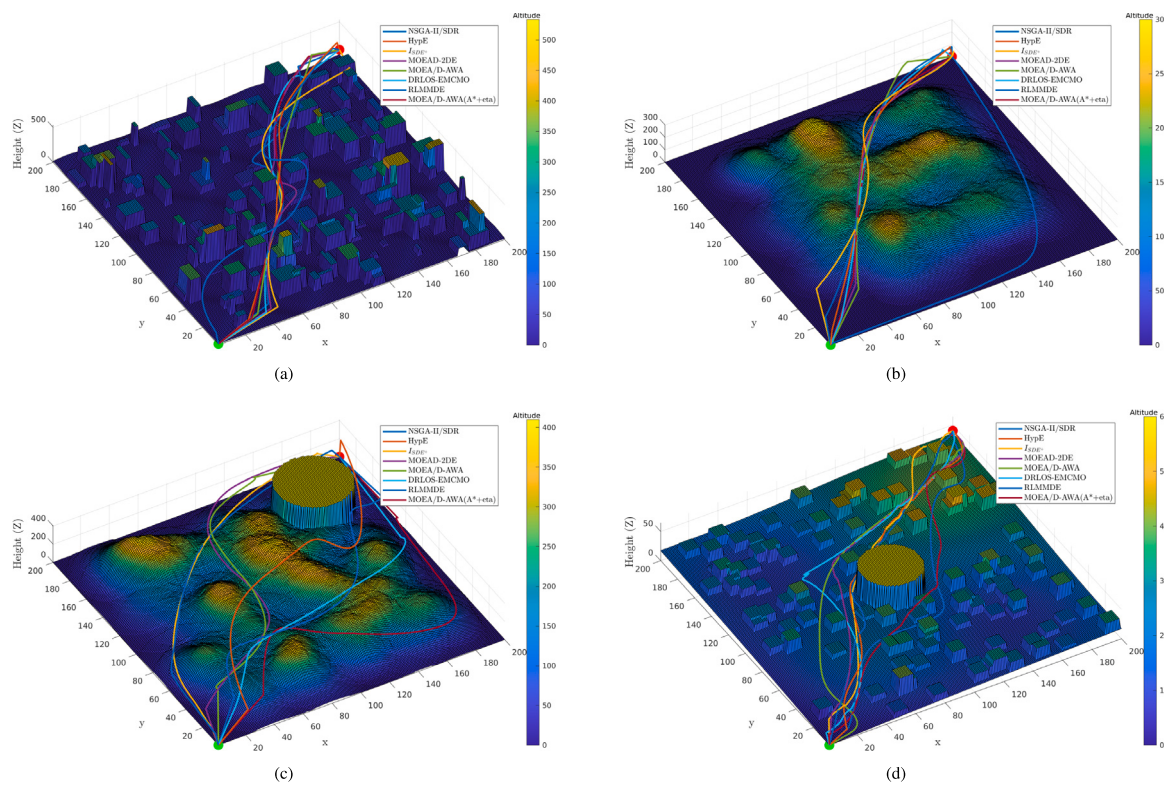


Fig. 5. UAV trajectories for compared algorithms: (a) dense-city C2 (no NFZ), (b) rugged mountains M2 (no NFZ), (c) mountain M6 with NFZ, and (d) suburban S4 with scattered buildings and NFZ. The proposed MOEA/D-AWA_{A*+η} consistently yields shorter, smoother, and constraint-compliant paths versus all baselines.

confined urban corridors. Unlike traditional algorithms such as NSGA-II/SDR or HypE, which often produce indirect or overly conservative routes, the proposed method maintains a smooth, low-altitude trajectory that minimizes path length while avoiding obstacles with precision. The reinforcement-learning-based algorithms, DRLOS-EMCMO and RLMMDE, show moderate adaptability through learned operator selection and reference adjustment mechanisms, yet their trajectories remain comparatively less direct, indicating that generalized learning strategies are insufficient to fully capture the geometric structure and environmental semantics that A*-guided operators exploit.

In the mountainous terrain without NFZs (M2, Fig. 5(b)), MOEA/D-AWA_{A*+η} again exhibits superior performance, producing well-optimized flight paths that effectively balance elevation control and trajectory smoothness. The algorithm dynamically adjusts its path to minimize steep ascents and descents, thereby reducing potential energy expenditure while preserving obstacle clearance. In contrast, MOEA-2DE and RLMMDE tend to overcompensate during elevation transitions, resulting in unnecessarily prolonged or oscillatory paths. DRLOS-EMCMO occasionally discovers feasible routes but displays inconsistent smoothness across runs due to stochastic operator selection inherent in its learning-driven framework. Classical algorithms such as HypE and I_{SDE+} , though competitive in flat regions, are less capable of managing steep or irregular topographies, leading to trajectories that are both longer and less energy-efficient. The superior results of MOEA/D-AWA_{A*+η} can be attributed to its integrated heuristic awareness, which enables the evolutionary process to reason spatially and adapt its search behavior to the underlying terrain.

In the more complex environments featuring NFZ constraints such as the mountainous region M6 (Fig. 5(c)) and the suburban setting S4 (Fig. 5(d)) MOEA/D-AWA_{A*+η} consistently delivers trajectories that are shorter, smoother, and fully compliant with airspace restrictions. The A*-guided variation operators facilitate precise path redirection around NFZs, while the adaptive mutation index enhances local refinement near feasible boundaries. Competing algorithms, including DRLOS-EMCMO and RLMMDE, exhibit partial constraint adherence but tend

to generate detours or abrupt altitude shifts due to the absence of explicit geometric modeling in their learning policies. Traditional evolutionary baselines, meanwhile, often produce irregular or infeasible solutions when confronted with dense constraint regions. These visual outcomes reinforce the earlier quantitative findings on hypervolume and path-quality metrics, collectively demonstrating that MOEA/D-AWA_{A*+η} achieves a uniquely effective balance between feasibility, efficiency, and robustness—attributes that make it particularly well-suited for real-world UAV path planning under heterogeneous and constraint-rich operational conditions.

6.6. Time complexity analysis

To complement the convergence and performance analyses, a comparative time-complexity evaluation was conducted following the standard procedure of the CEC benchmark series. The computational assessment involved (i) establishing a baseline execution time T_0 using a predefined arithmetic-transcendental loop, (ii) measuring the time T_1 required for the evaluation of a single individual, and (iii) recording the total runtime T_2 for each algorithm executing 10,000 iterations, averaged over 30 independent runs to obtain \bar{T}_2 . The normalized complexity measure ($\bar{T}_2 - T_1$)/ T_0 thus reflects the relative computational overhead attributable to algorithmic structure rather than hardware-specific factors.

Fig. 6 presents the average runtime ranks for four representative benchmark problems—C1 (urban), S2 (suburban), M2 (mountainous), and M6 (highly rugged mountainous). As shown, MOEA/D-AWA_{A*+η} consistently exhibits the highest runtime across all evaluated problems. This increased computational cost stems primarily from the integration of domain-aware A*-guided crossover and mutation operators, which require additional path feasibility checks and geometric computations at each offspring generation stage. Furthermore, the adaptive mutation index introduces dynamic parameter adjustments that compound the

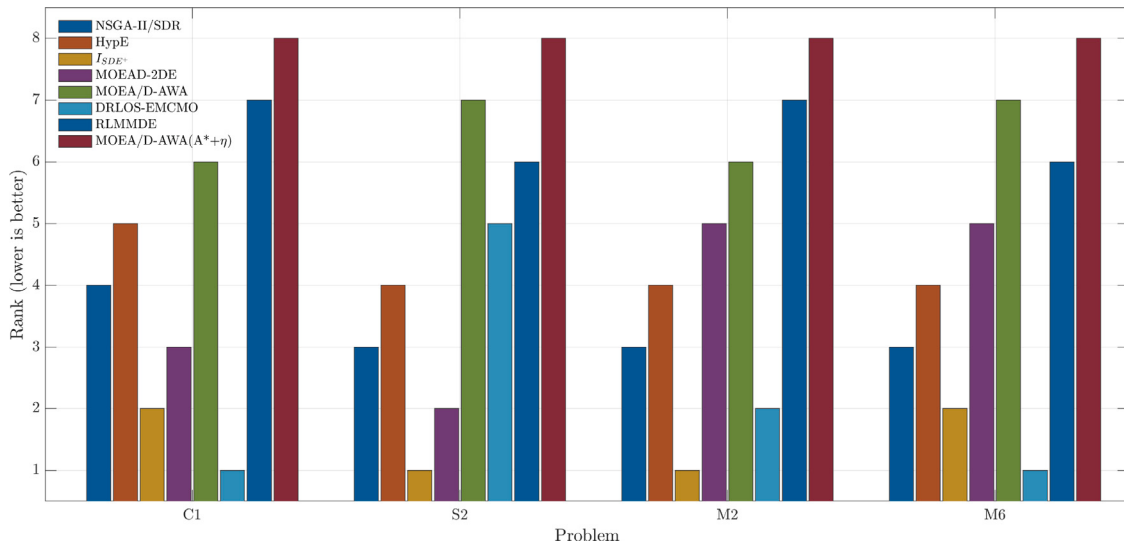


Fig. 6. Average runtime ranks of the compared algorithms across four representative benchmark problems: C1 (urban), S2 (suburban), M2 (mountainous), and M6 (rugged mountainous). A lower rank indicates faster execution.

overall processing time per iteration. These operations, while computationally intensive, play a critical role in steering the search toward feasible and high-quality regions of the decision space.

It is important to note, however, that the computational cost of MOEA/D-AWA $A^{*+\eta}$ is broadly in line with several recent learning-based approaches, such as RLMMDE, which also incur higher runtimes due to policy updates, reward evaluation, and environment interaction overheads. In contrast, while methods like NSGA-II/SDR and HypE achieve faster execution times, they do so at the expense of convergence stability and path-quality performance. The runtime behavior of our algorithm is therefore not atypical but rather consistent with that of advanced learning-driven or hybrid optimization frameworks that balance deeper exploration with improved solution robustness. Despite the elevated runtime, the observed performance–cost trade-off remains decisively favorable. As demonstrated in Sections 6.1–6.5, MOEA/D-AWA $A^{*+\eta}$ consistently outperforms all competitors in terms of hypervolume, convergence stability, and practical path-quality metrics—achieving up to 98% improvement in obstacle-aware flight paths relative to its base variant. The higher time complexity is therefore justified as a necessary trade-off for enhanced constraint awareness and informed search behavior rather than a symptom of algorithmic inefficiency.

Overall, these findings confirm that MOEA/D-AWA $A^{*+\eta}$ achieves a principled balance between computational expense and optimization quality. The added complexity reflects a well-founded design compromise that enables robust convergence, superior trajectory generation, and operational reliability—qualities that are critical for real-world UAV path planning, where safety and performance take precedence over marginal gains in runtime.

7. Conclusion and future works

In this study, we introduced and evaluated novel heuristic-driven evolutionary operators, specifically the A*-guided waypoint-connecting crossover, the A*-guided mutation, and an adaptive polynomial mutation strategy (η), within the existing MOEA/D-AWA algorithm. The operators were applied to multi-objective UAV path-planning problems encompassing diverse environments, including urban, suburban, and mountainous terrains characterized by varying obstacle complexities and no-fly zones. Empirical results demonstrated that incorporating these heuristic-based operators substantially enhanced the performance of MOEA/D-AWA, consistently outperforming benchmark algorithms

(NSGA-II/SDR, HypE, I_{SDE+} , MOEA-2DE, and the original MOEA/D-AWA) in terms of hypervolume, convergence speed, and solution robustness.

The effectiveness of the proposed operators stems from their ability to guarantee path feasibility inherently through A*-guided local search, combining efficient global exploration with precise local optimization. Furthermore, the adaptive polynomial mutation dynamically adjusted mutation intensity according to evolutionary progress, effectively balancing exploration and exploitation at various evolutionary stages. Trajectory visualizations further validated these quantitative improvements, illustrating superior obstacle avoidance and more efficient, smooth trajectories across benchmark scenarios.

Future work includes extending these heuristic-based operators to address dynamic and uncertain environments, exploring their integration into cooperative multi-UAV path-planning contexts, and incorporating more realistic UAV operational constraints, such as energy efficiency, wind disturbance modeling, and communication limitations. Furthermore, in the current study path planning has been evaluated under static obstacle configurations. While this provides a rigorous basis for testing multi-objective optimization performance, it does not capture the full range of UAV operational characteristics where obstacles may evolve or emerge over time. Extending these operators to dynamic and time-varying settings, together with online re-planning strategies (e.g., rolling-horizon evolutionary optimization or model-predictive control), represents a natural and important continuation of this work. We note that, although waypoint-level feasibility is strictly enforced, B-spline smoothing does not provide a theoretical guarantee of collision-free interpolation along the entire continuous path. In extremely cluttered environments, minor violations may still occur. Enhancing the smoothing stage with collision-aware spline refinement or free-space corridor enforcement will therefore be an important direction for future investigation.

An additional consideration is the scalability of the framework to real UAV missions. While the benchmarks used are simulated, they were designed to reflect realistic geometric and regulatory complexities (e.g., clustered urban obstacles, no-fly zones, and rugged terrain). These environments establish a challenging yet reproducible foundation for validating operator effectiveness. In practical deployments, additional challenges such as sensor uncertainty, dynamic obstacles, and communication constraints will arise. The proposed operators are directly compatible with such settings, as the A*-guided heuristics ensure trajectory feasibility under evolving constraints, while the adaptive mutation mechanism naturally adjusts search pressure throughout the

evolutionary process. Embedding these operators within parallelized, surrogate-assisted, or online cooperative re-planning schemes could further enhance scalability, facilitating their application in large-scale and real-world UAV missions.

CRediT authorship contribution statement

Daison Darlan: Writing – review & editing, Writing – original draft, Visualization, Software, Methodology, Investigation, Formal analysis, Conceptualization. **Oladayo S. Ajani:** Writing – review & editing, Validation, Methodology, Investigation, Conceptualization. **Rammo-han Mallipeddi:** Writing – review & editing, Validation, Supervision, Resources, Investigation, Conceptualization.

Declaration of competing interest

The authors hereby declare that there are no conflicts of interest related to the research, authorship, and/or publication of this article. No financial or personal relationships exist that could have inappropriately influenced or biased the work presented in this manuscript.

Acknowledgment

This research was supported by the Core Research Institute Basic Science Program through the National Research Foundation of Korea (NRF) funded by the Ministry of Education (RS-2021-NR060127).

Appendix A. Supplementary data

Supplementary material related to this article can be found online at <https://doi.org/10.1016/j.swevo.2025.102267>.

Data availability

The code and resources used in this study are publicly available at <https://github.com/Anomaly33/Heuristic-Driven-Evolutionary-UAV-Path-Planning>. This repository includes implementations for evolutionary operators designed in this work, benchmark problem instances, and UAV path-planning algorithms.

References

- [1] X. Li, A.V. Savkin, Networked unmanned aerial vehicles for surveillance and monitoring: A survey, *Future Internet* 13 (7) (2021) 174.
- [2] A. Chriki, H. Touati, H. Snoussi, F. Kamoun, Uav-based surveillance system: an anomaly detection approach, in: 2020 IEEE Symposium on Computers and Communications, ISCC, IEEE, 2020, pp. 1–6.
- [3] M. Sajid, H. Mittal, S. Pare, M. Prasad, Routing and scheduling optimization for UAV assisted delivery system: A hybrid approach, *Appl. Soft Comput.* 126 (2022) 109225.
- [4] J. Li, H. Liu, K.K. Lai, B. Ram, Vehicle and UAV collaborative delivery path optimization model, *Mathematics* 10 (20) (2022) 3744.
- [5] S. Ghambari, M. Golabi, L. Jourdan, J. Lepagnot, L. Idoumghar, UAV path planning techniques: a survey, *RAIRO-Oper. Res.* 58 (4) (2024) 2951–2989.
- [6] X. Xu, C. Xie, Z. Luo, C. Zhang, T. Zhang, A multi-objective evolutionary algorithm based on dimension exploration and discrepancy evolution for UAV path planning problem, *Inform. Sci.* 657 (2024) 119977.
- [7] Y. Wan, Y. Zhong, A. Ma, L. Zhang, An accurate UAV 3-D path planning method for disaster emergency response based on an improved multiobjective swarm intelligence algorithm, *IEEE Trans. Cybern.* 53 (4) (2022) 2658–2671.
- [8] M. Jones, S. Djahel, K. Welsh, Path-planning for unmanned aerial vehicles with environment complexity considerations: A survey, *ACM Comput. Surv.* 55 (11) (2023) 1–39.
- [9] R. Perez-Segui, P. Arias-Perez, J. Melero-Deza, M. Fernandez-Cortizas, D. Perez-Saura, P. Campoy, Bridging the gap between simulation and real autonomous uav flights in industrial applications, *Aerospace* 10 (9) (2023) 814.
- [10] K. Deb, A. Pratap, S. Agarwal, T. Meyarivan, A fast and elitist multiobjective genetic algorithm: NSGA-II, *IEEE Trans. Evol. Comput.* 6 (2) (2002) 182–197.
- [11] Q. Zhang, H. Li, MOEA/D: A multiobjective evolutionary algorithm based on decomposition, *IEEE Trans. Evol. Comput.* 11 (6) (2007) 712–731.
- [12] C. Peng, S. Qiu, A decomposition-based constrained multi-objective evolutionary algorithm with a local infeasibility utilization mechanism for UAV path planning, *Appl. Soft Comput.* 118 (2022) 108495.
- [13] J. Luo, Y. Tian, Z. Wang, Research on unmanned aerial vehicle path planning, *Drones* 8 (2) (2024) 51.
- [14] G. Gugan, A. Haque, Path planning for autonomous drones: Challenges and future directions, *Drones* 7 (3) (2023) 169.
- [15] J. Xie, J. Chen, Multiregional coverage path planning for multiple energy constrained UAVs, *IEEE Trans. Intell. Transp. Syst.* 23 (10) (2022) 17366–17381.
- [16] T. Quadt, R. Lindelauf, M. Voskuijl, H. Monsuur, B. Čule, Dealing with multiple optimization objectives for UAV path planning in hostile environments: A literature review, *Drones* (2504-446X) 8 (12) (2024).
- [17] M. Hamdan, A dynamic polynomial mutation for evolutionary multi-objective optimization algorithms, *Int. J. Artif. Intell. Tools* 20 (01) (2011) 209–219.
- [18] P.E. Hart, N.J. Nilsson, B. Raphael, A formal basis for the heuristic determination of minimum cost paths, *IEEE Trans. Syst. Sci. Cybern.* 4 (2) (1968) 100–107.
- [19] D. Darlan, O.S. Ajani, A. Paul, R. Mallipeddi, A multi-objective benchmark for UAV path planning with baseline results, *Swarm Evol. Comput.* 96 (2025) 101968.
- [20] F. Yang, L. Xu, X. Chu, S. Wang, A new dominance relation based on convergence indicators and niching for many-objective optimization, *Appl. Intell.* (2021) 1–18.
- [21] J. Bader, E. Zitzler, HypE: An algorithm for fast hypervolume-based many-objective optimization, *Evol. Comput.* 19 (1) (2011) 45–76.
- [22] T. Pamulapati, R. Mallipeddi, P.N. Suganthan, ISDE+—an indicator for multi and many-objective optimization, *IEEE Trans. Evol. Comput.* 23 (2) (2018) 346–352.
- [23] Y. Qi, X. Ma, F. Liu, L. Jiao, J. Sun, J. Wu, MOEA/D with adaptive weight adjustment, *Evol. Comput.* 22 (2) (2014) 231–264.
- [24] Q. Ren, Y. Yao, G. Yang, X. Zhou, Multi-objective path planning for UAV in the urban environment based on CDNSGA-II, in: 2019 IEEE International Conference on Service-Oriented System Engineering, SOSE, IEEE, 2019, pp. 350–3505.
- [25] X. Zhen, Z. Enze, C. Qingwei, Rotary unmanned aerial vehicles path planning in rough terrain based on multi-objective particle swarm optimization, *J. Syst. Eng. Electron.* 31 (1) (2020) 130–141.
- [26] Y. Xiao, H. Yang, H. Liu, K. Wu, G. Wu, UAV 3-D path planning based on MOEA/D with adaptive areal weight adjustment, *IEEE Trans. Aerosp. Electron. Syst.* (2024).
- [27] J. Guo, Y. Wan, A. Ma, Y. Zhong, A global-local collaborative and decomposition-based multi-objective evolutionary optimization method for UAV 3-D path planning, *IEEE Internet Things J.* (2025).
- [28] Z. Ren, C. Hernández, M. Likhachev, A. Felner, S. Koenig, O. Salzman, S. Rathinam, H. Choset, EMOA*: A framework for search-based multi-objective path planning, *Artificial Intelligence* 339 (2025) 104260.
- [29] W. Zhang, C. Peng, Y. Yuan, J. Cui, L. Qi, A novel multi-objective evolutionary algorithm with a two-fold constraint-handling mechanism for multiple UAV path planning, *Expert Syst. Appl.* 238 (2024) 121862.
- [30] G. Huang, M. Hu, X. Yang, Y. Wang, P. Lin, A two-stage co-evolution multi-objective evolutionary algorithm for UAV trajectory planning, *Appl. Sci.* 14 (15) (2024) 6516.
- [31] J. Guo, Y. Wan, A. Ma, Y. Zhong, Disaster-aware path planning based on reinforcement learning for post-earthquake emergency response, *IEEE Trans. Geosci. Remote Sens.* (2025).
- [32] Y. Guo, Z. Liu, UAV Path Planning Based on Deep Reinforcement Learning, Monitoring and Control (ANMC) Cooperate: Xi'an Technological University (CHINA) West Virginia University (USA) Huddersfield University of UK (UK), 2023, p. 81.
- [33] J. Li, Y. Hu, S.X. Yang, A novel knowledge-based genetic algorithm for robot path planning in complex environments, *IEEE Trans. Evol. Comput.* (2025).
- [34] J. Zhu, D. Pan, Improved genetic algorithm for solving robot path planning based on grid maps, *Mathematics* 12 (24) (2024) 4017.
- [35] N. Hohmann, M. Bujny, J. Adamy, M. Olhofer, Hybrid evolutionary approach to multi-objective path planning for UAVs, in: 2021 IEEE Symposium Series on Computational Intelligence, SSCI, IEEE, 2021, pp. 1–8.
- [36] Y. Hu, S.X. Yang, A knowledge based genetic algorithm for path planning of a mobile robot, in: IEEE International Conference on Robotics and Automation, 2004. Proceedings. ICRA'04. 2004, Vol. 5, IEEE, 2004, pp. 4350–4355.
- [37] Q. Shen, D. Zhang, Q. He, Y. Ban, F. Zuo, A novel multi-objective dung beetle optimizer for Multi-UAV cooperative path planning, *Heliyon* 10 (17) (2024).
- [38] H.-c. Sang, S.-j. Song, X.-p. Xing, Y. Meng, Z. Zhang, M. Tang, Application of adaptive genetic algorithm in robot path planning, *J. Xi'an Polytech. Univ.* 35 (2021) 44–49.
- [39] R. Jarray, M. Al-Dhaifallah, H. Rezk, S. Bouallègue, Parallel cooperative coevolutionary grey wolf optimizer for path planning problem of unmanned aerial vehicles, *Sensors* 22 (5) (2022) 1826.
- [40] Q. Meng, Q. Qu, K. Chen, T. Yi, Multi-UAV path planning based on cooperative co-evolutionary algorithms with adaptive decision variable selection, *Drones* (2504-446X) 8 (9) (2024).
- [41] Y. Jiang, X.-X. Xu, M.-Y. Zheng, Z.-H. Zhan, Evolutionary computation for unmanned aerial vehicle path planning: A survey, *Artif. Intell. Rev.* 57 (10) (2024) 267.

- [42] C.C. Coello, M.S. Lechuga, MOPSO: A proposal for multiple objective particle swarm optimization, in: Proceedings of the 2002 Congress on Evolutionary Computation. CEC'02 (Cat. No. 02TH8600), Vol. 2, IEEE, 2002, pp. 1051–1056.
- [43] H. Qiu, H. Duan, A multi-objective pigeon-inspired optimization approach to UAV distributed flocking among obstacles, *Inform. Sci.* 509 (2020) 515–529.
- [44] R. Van Hoek, J. Ploeg, H. Nijmeijer, Cooperative driving of automated vehicles using B-splines for trajectory planning, *IEEE Trans. Intell. Veh.* 6 (3) (2021) 594–604.
- [45] A. Gasparetto, P. Boscaroli, A. Lanzutti, R. Vidoni, Path planning and trajectory planning algorithms: A general overview, in: Motion and Operation Planning of Robotic Systems: Background and Practical Approaches, Springer, 2015, pp. 3–27.
- [46] J.L. Foo, J. Knutzon, V. Kalivarapu, J. Oliver, E. Winer, Path planning of unmanned aerial vehicles using B-splines and particle swarm optimization, *J. Aerosp. Comput. Inf. Commun.* 6 (4) (2009) 271–290.
- [47] M. Hamdan, The distribution index in polynomial mutation for evolutionary multiobjective optimisation algorithms: An experimental study, in: International Conference on Electronics Computer Technology, IEEE, Kanyakumari, India, 2012, 2012.
- [48] J.L. Carles-Bou, S.F. Galán, Self-adaptive polynomial mutation in NSGA-II, *Soft Comput.* 27 (23) (2023) 17711–17727.
- [49] R. Tinós, S. Yang, Self-adaptation of mutation distribution in evolutionary algorithms, in: 2007 IEEE Congress on Evolutionary Computation, IEEE, 2007, pp. 79–86.
- [50] X. Yao, Y. Liu, G. Lin, Evolutionary programming made faster, *IEEE Trans. Evol. Comput.* 3 (2) (1999) 82–102.
- [51] Y. Han, H. Peng, C. Mei, L. Cao, C. Deng, H. Wang, Z. Wu, Multi-strategy multi-objective differential evolutionary algorithm with reinforcement learning, *Knowl.-Based Syst.* 277 (2023) 110801.
- [52] F. Ming, W. Gong, L. Wang, Y. Jin, Constrained multi-objective optimization with deep reinforcement learning assisted operator selection, *IEEE/CAA J. Autom. Sin.* 11 (4) (2024) 919–931.
- [53] Y. Ren, Y. Gao, W. Xu, C.-M. Chen, M. Amoon, Variable grid-based path-planning approach for UAVs in air-ground integrated network, *Trans. Emerg. Telecommun. Technol.* 36 (11) (2025) e70276.
- [54] D. Debnath, F. Vanegas, J. Sandino, A.F. Hawary, F. Gonzalez, A review of UAV path-planning algorithms and obstacle avoidance methods for remote sensing applications, *Remote Sens.* 16 (21) (2024) 4019.
- [55] R. Kabir, Y. Watanobe, M.R. Islam, K. Naruse, Enhanced robot motion block of a-star algorithm for robotic path planning, *Sensors* 24 (5) (2024) 1422.
- [56] H. Seada, M. Abouhawwash, K. Deb, Towards a better balance of diversity and convergence in NSGA-III: First results, in: Evolutionary Multi-Criterion Optimization: 9th International Conference, EMO 2017, Münster, Germany, March 19–22, 2017, Proceedings 9, Springer, 2017, pp. 545–559.
- [57] H. Ishibuchi, Y. Sakane, N. Tsukamoto, Y. Nojima, Evolutionary many-objective optimization by NSGA-II and MOEA/D with large populations, in: 2009 IEEE International Conference on Systems, Man and Cybernetics, IEEE, 2009, pp. 1758–1763.